Pergamon

Geochimica et Cosmochimica Acta, Vol. 67, No. 14, pp. 2631–2647, 2003

0016-7037/03 $30.00 + .00

doi:10.1016/S0016-7037(00)00199-6

Control of sulfate pore-water profiles by sedimentary events and the significance of anaerobic oxidation of methane for the burial of sulfur in marine sediments

Christian Hensen,[1,*] Matthias Zabel,[1] Kerstin Pfeifer,[1] Tilmann Schwenk,[1] Sabine Kasten,[1] Natascha Riedinger,[1] Horst D. Schulz,[1] and Antje Boetius[2]

[1]Fachbereich Geowissenschaften, Universität Bremen, Klagenfurter Strasse, 28359 Bremen, Germany
[2]Max-Planck Institute for Marine Microbiology, Celsiusstrasse 1, 28359 Bremen, Germany

(*Received July* 2, 2002; *accepted in revised form March* 5, 2003)

Abstract—Gravity driven mass-flow deposits proven by sedimentary and digital echosounder data are indicative for prevailing dynamic sedimentary conditions along the continental margin of the western Argentine Basin. In this study we present geochemical data from a total of 23 gravity cores. Pore-water SO_4 is generally depleted within a few meters below the sediment surface by anaerobic oxidation of methane (AOM). The different shapes of SO_4 profiles (concave, kink- and s-type) can be consistently explained by sedimentary slides possibly in combination with changes in the CH_4 flux from below, thus, mostly representing transient pore-water conditions. Since slides may keep their original sedimentary signature, a combined analysis and numerical modeling of geochemical, physical properties, and hydro acoustic data could be applied in order to reconstruct the sedimentary history. We present first order estimates of the dating of sedimentary events for an area where conventional stratigraphic methods failed to this day. The results of the investigated sites suggest that present day conditions are the result of events that occurred decades to thousands of years ago and promote a persisting mass transport from the shelf into the deep-sea, depositing high amounts of reactive compounds. The high abundance of reactive iron phases in this region maintains low hydrogen sulfide levels in the sediments by a nearly quantitative precipitation of all reduced sulfate by AOM. For the total region we estimate a SO_4 (or CH_4) flux of 6.6×10^{10} moles per year into the zone of AOM. Projected to the global continental slope and rise area, this may sum up to about 2.6×10^{12} moles per year. Provided that the sulfur is completely fixed in the sediments it is about twice the global value of the recent global sulfur burial in marine sediments of 1.2×10^{12} moles per year as previously estimated. Thus, AOM obviously contributes very significantly to the regulation of global sulfur reservoirs, which is hitherto not sufficiently recognized. This finding may have implications for global geochemical models, as sulfur burial is an important control factor in the development of atmospheric oxygen levels over time.

1. INTRODUCTION

In continental margin sediments below the upper few decimeters of the surface sediments the metabolic activity is dominated by sulfate reduction and methanogenesis (D'Hondt et al., 2002). Whereas sulfate reduction rates (SRR) are highest close to the sediment surface due to the better degradability of organic material the final depletion of SO_4 is attributed to anaerobic oxidation of methane (AOM; e.g., Fossing et al., 2000; Jørgensen et al., 2001). Because the zone of AOM is usually located a few meters below the sediment surface, the latter is governed by the much longer distance between the bottom water source of SO_4 and the reaction zone. Recent studies have shown that ~100% of the downward SO_4 flux goes into AOM (Borowski et al., 1996; Niewöhner et al., 1998) emphasizing the significance of this process as an important sink for the effective greenhouse gas CH_4. Thus, the availability of SO_4 in the sediment and the location of the zone of AOM are significantly dependent on the production and the flux of CH_4 from below. The supply may occur either by diffusion or by fluid advection and bubble ebullition at cold seeps. Additionally, huge amounts of CH_4 can be stored in form of gas hydrates and their destabilization may provide additional sources, possibly leading to catastrophic events like tsunamis by triggering giant submarine landslides and megaturbidites (Dawson, 1988; Young, 1992).

Extensive studies related to the AOM have been conducted in shallow marine and extreme environments (mostly related to fluid seepage sites) to enhance the understanding of this complex, microbially controlled process and to evaluate its quantitative importance (e.g., Iversen and Jørgensen, 1985; Ferdelman et al., 1997; Suess et al., 1999; Boetius et al., 2000; Michaelis et al., 2002). A major step in this regard was the discovery of a "consortium" of archaea and SO_4 reducers mediating the CH_4 oxidation in sediments of the Cascadia continental margin (Boetius et al., 2000), a mechanism, which was already suggested by other researchers (Hoehler et al., 1994; Hinrichs et al., 1999). However, only a few studies up to now are concerned with the process in the deep marine environment away from active seeping sites (Niewöhner et al., 1998; Borowski et al., 1999; Fossing et al., 2000; Dickens, 2001; Zabel and Schulz, 2001). Thus, neither much is known about the magnitude and the control mechanisms that drive AOM in the deeper parts of the ocean nor how important it is concerning the global budgets of C and S. However, variations of the environmental parameters that determine steady-state conditions have significant impact on stationarity of the geochemical system, which will tend to re-equilibrate again. Dickens (2001) demonstrated that the Holocene sea-level rise may

* Author to whom correspondence should be addressed, at SFB 574, GEOMAR, Forschungszentrum für Marine Geowissenschaften, Wischhofstrasse 1-3, 24148, Kiel, Germany (chensen@geomar.de).

have increased gas hydrate stability inducing reduced rates of AOM and non-stationary pore-water profiles of sulfate. Episodic sedimentary events like turbidites triggering non-steady state conditions in combination with a decreased Holocene export production are reported from various sites of the oligotrophic eastern Atlantic or the Madeira Abyssal Plain (Thomson et al., 1984; Wilson et al., 1986; Wilson and Thomson, 1998). The sedimentary dynamics induced downward prograding oxidation fronts favored by the C-limitation of the surface sediments and are associated by the characteristic formation of Fe- and Mn-rich layers Wilson et al. (1985). By application of a simple numerical model Wilson et al. (1986) were able to calculate the time that has elapsed since the deposition of a turbidite and they could reasonably reproduce observed associated enrichments of Mn- and Fe-oxides. Similarly, the "burn-down" of oxygen is well known from the recent S1-sapropel in the eastern Mediterranean Sea, where it is attributed to the Holocene shift from a high productivity situation associated with low bottom water oxygen levels to oligotrophic production and well oxygenated bottom water conditions (Pruysers et al., 1993; Thomson et al., 1995; Van Santvoort et al., 1996). The cyclic deposition of sapropels and normal marine sediments during the Neogene also implicated changes from oxic to anoxic conditions. Pyrite enrichments below the sapropels formed by downward diffusion of surplus H_2S below the subsurface are a conspicuous feature that repeatedly occurred during high productivity phases in the eastern Mediterranean (Passier et al., 1996). Non-steady state diagenetic conditions are also reported from the Baltic Sea, the Black Sea and Indonesia, where changes from limnic or brackish conditions to organic-rich marine depositions caused postdepositional sulfide enrichments within non-marine sequences (Boesen and Postma, 1988; Middelburg, 1991; Middelburg et al., 1991).

The continental slope region of Argentina, Uruguay, and southern Brazil is a unique study area for combined biogeochemical and sedimentological studies with respect to AOM-driven sulfate reduction and non-steady state diagenesis. This is because of (1) the prevailing, dynamic conditions in the surface waters causing a high overall primary productivity (e.g., Behrenfeld and Falkowski, 1997) and export of organic material to the sea floor, (2) massive downslope transport of material by slides and turbidity currents from the continental shelf leading to increased sedimentation on the slope and in the basin (Ewing et al., 1964; Ledbetter and Klaus, 1987), and (3) sediment dispersal and re-distribution by bottom currents (Ewing et al., 1971; Richardson et al., 1993). The specific focus of this study is to show how SO_4 pore-water profiles are affected by sedimentary events and that resulting transient pore-water conditions are a ubiquitous feature. In addition, scenarios based on a combined analysis of geochemical and geophysical data are presented demonstrating the possibility of using non-steady state conditions for the dating of sedimentary events. Finally, we discuss the quantitative significance of AOM for the sulfur budget in marine sediments.

2. MATERIALS AND METHODS

2.1. Oceanographic and Sedimentary Conditions of the Study Area

The western part of the Argentine Basin is characterized by rather specific oceanographic conditions. The dynamics of the upper water column are mainly governed by the interaction of the Brazil and Malvinas (Falklands) Currents, and their confluence at ~35–38°S (Brazil-Malvinas Confluence, BMC) located in front of the Rio de la Plata (Gordon, 1989; Peterson and Stramma, 1991). The intense mixing of tropical and Antarctic waters in the BMC system produces sharp horizontal and vertical gradients of temperature, salinity, and nutrients, which are highly variable in space and time (Gordon, 1989). These conditions are favorable for the formation of eddies and filaments (Wilson and Rees, 2000) thus increasing levels of primary productivity in the surface water up to 250 gC m^{-2} yr^{-1} over a large area (Antoine et al., 1996; Behrenfeld and Falkowski, 1997). High flow velocity-conditions extending to the sea floor are also responsible for winnowing and re-distribution of dominantly terrigeneous sediments on the shelf and the upper continental margin, which are discharged, in large amounts by the Rio de la Plata and other tributaries along the Argentine coast (Garzoli, 1993; Peterson et al., 1996). However, the BMC marks not only a rapid transition between upper-level current regimes, but it is also at the crossroads of a number of major water masses (Reid, 1989). Especially, below 4000 m water depth the Antarctic Bottom Water (AABW) forms a strong contour current along the continental margin flowing from south to north taking up and delivering fine grained sediments far into the central basin, where thick nepheloid layers and mud waves are formed (Ewing et al., 1971; Ledbetter and Klaus, 1987; Richardson et al., 1993). Overall, huge amounts of sediment are transported from the shelf area downslope into the basin which is strongly reflected by surface sediment composition and benthic mineralization rates: (1) the sediments are depleted in $CaCO_3$, but have high organic carbon (C_{org}) and biogenic opal concentrations, (2) the C_{org} and benthic mineralization rates are highest at midslope depths between 2500–3500 m (development of a depo-center by downslope processes), (3) opal contents and benthic silica release are highest at depths below 4000 m due to the supply of benthic diatoms by the AABW, (4) the overall pattern of benthic mineralization rates is similar to that of biogenic opal, and (5) the distribution of major diatom groups (specifically benthic diatoms) reflects the major area of downslope processes in this area (Hensen et al., 2000, in press; Romero and Hensen, 2002). Reliable stratigraphic information for this region does not exist. However, a preliminary on-board stratigraphy based on *Globorotalia menardii* indicate, that Holocene sediments on top are often missing (Segl and participants, 1994). The reasons for this may be erosional processes or sediment mixing, low carbonate contents or simply the application of a method (thought for tropical regions) out of their normal longitudinal limits.

2.2. Sampling and Sample Processing

All 23 gravity cores investigated in this study were collected during the expeditions M 29-1/2 (1994) and M 46-2/3 (1999–2000) with RV *Meteor* in the Southwestern Atlantic located between 27°S to 50°S and 38° to 68°W (Table 1, Fig. 1). At each location a second core was taken. All physical properties data shown below are from these parallel cores.

Below we give only a short outline of sampling procedures and analyses techniques. A complete overview of the techniques is available on http://www.geochemie.uni-bremen.de (or see Schulz et al., 1994; Haese et al., 1997; Hensen et al., 1998; Niewöhner et al., 1998).

After retrieval on board, the cores were cut in 1 m segments and syringe samples (only M 46-2) were taken on deck from every cut segment surface for preliminary CH_4 analysis. To prevent further warming of the sediments the cores were subsequently placed in a cooling laboratory and maintained at a temperature of ~4°C. On cruise M 46-2 a higher resolution sampling for CH_4 analysis was carried out immediately after storing. Generally, the cores were cut lengthwise within the first 2 d after recovery and sediment samples were taken for pressure filtration of the pore-water (20–25 cm), and subsequent analyses of the solid phase (kept in gas-tight glass bottles under anoxic atmosphere). The storage temperature for all sediments was −20°C to suppress subsequent alteration processes. All work done on opened cores was carried out in a glove box under argon atmosphere. For pressure filtration Teflon- and PE-squeezers were used. The squeezers were operated with argon at a pressure gradually increasing up to 5 bars. The pore-water was retrieved through 0.2 μm cellulose acetate membrane filters. Phosphate was measured photometrically with help

Table 1. Compilation of the station numbers, geographic positions, and water depths of all gravity cores used for this study. The penetration depths as well as the diffusive fluxes of SO_4 are discussed in the text.

Station	Longitude (°)	Latitude (°)	Water depth (m)	SO_4 penetration depth (m)	SO_4 diffusive flux (mmol m^{-2} yr^{-1})[a]
2704-2	−53.92	−38.92	3247	10.0	21.79
2707-5	−56.32	−41.95	3167	14.0	14.69
2712-3	−59.33	−43.68	1228	10.5	19.05
2714-1	−57.99	−43.87	2361	45[b]	6.00
2716-2	−56.98	−44.00	4624	20[b]	11.24
2718-4	−58.18	−47.31	2990	105[b]	3.53
2722-4	−58.62	−47.33	2351	20[b]	9.60
2724-4	−56.17	−47.95	4799	12.0	17.87
2803-3	−53.71	−37.41	1162	40[b]	6.67
2806-5	−53.14	−37.83	3542	3.7	75.42
2809-4	−51.52	−36.33	3539	9.3	162.48
2811-2	−52.27	−35.75	1789	5.9	55.62
2825-2	−41.43	−32.50	4352	165[b]	1.01
2829-2	−43.43	−30.88	3523	220[b]	1.62
6202-6	−47.17	−29.09	1492	12.0	20.23
6206-2	−46.56	−30.21	2430	20[b]	10.29
6214-7	−51.44	−34.53	1568	4.9	84.60
6219-2	−50.57	−35.19	3551	4.1	93.30
6223-6	−49.68	−35.74	4280	5.1	43.52
6229-6	−52.65	−37.21	3551	5.6	39.92
6308-4	−53.97	−39.30	3623	5.0	43.11
6323-3	−48.26	−45.59	5480	35[b]	6.97
6330-4	−57.56	−46.15	3877	50[b]	6.32

[a] Calculated according to Fick's first law using a constant porosity of 75%.
[b] Estimated penetration depth.

of an autoanalyser using standard methods (Grasshoff et al., 1983). Alkalinity was calculated from a volumetric analysis by titration of 1–1.5 mL sample with 0.01–0.1 mol/L HCl. For the analysis of iron concentrations subsamples of 1 mL were taken within the glove box and immediately complexed with 20 μL of Ferrozin and afterwards determined photometrically. Subsamples for SO_4 determinations were diluted (1:20) and analyzed by ion chromatography (HPLC). For H_2S analyses at higher concentrations, 1 mL subsamples of the pore-water were added to a ZnAc-solution to fix all hydrogen sulfide present as ZnS and determined by ICP-AES techniques (Perkin Elmer Optima 3000 RL) in the home laboratory. For detection of CH_4 20 μL of the headspace gas was injected into a gas-chromatograph (Varian 3400) with a splitless injector. CH_4 concentrations were subsequently corrected for sediment porosity.

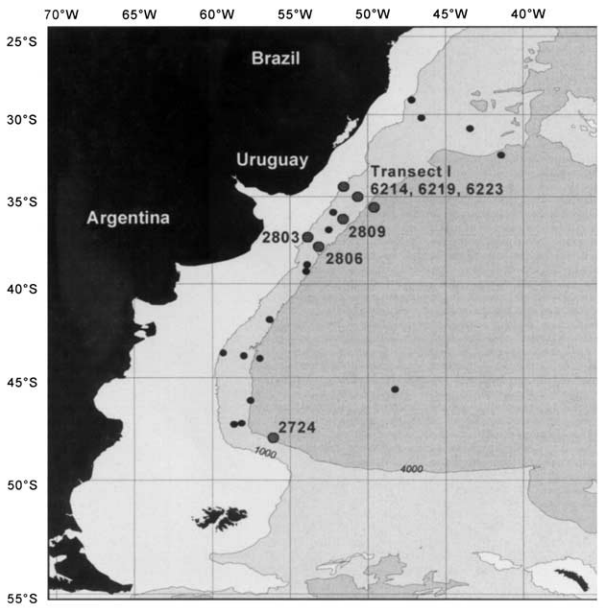

Fig. 1. Map of the western Argentine Basin showing the locations of all sampled gravity cores. Bold symbols indicate those locations, which are discussed in more detail.

Total digestions of the sediment and reactive Fe(III)-extractions were performed on anoxic subsamples. Reactive Fe(III)-concentrations were calculated as the sum of ascorbate and dithionite extractions following the method described by Haese et al. (1997).

Sulfate reduction rates (SRR) were determined on separate sediment samples applying the $^{35}SO_4$ incubation method (Jørgensen, 1977; Boetius et al., 2000).

During all cruises in the working area, the shipboard sediment echosounder system PARASOUND was used to record continuous high-resolution seismic profiles. The PARASOUND system utilizes the parametric effect leading to an excellent lateral resolution of 7% of water depth, whereas the vertical resolution is an order of a few decimeters (Grant and Schreiber, 1990). The seismograms were digitized and stored with the digital acquisition system PARADIGMA (Spiess, 1993). From all cruises a continuous high-frequency seismic record of the upper 10–100 m of surface sediments is available.

2.3. Geochemical Modeling

Transport and reaction modeling was performed with the computer software CoTReM, which is a modular, numerical, non-steady state model based on an operator splitting approach (detailed information concerning the concept and the use of CoTReM can be obtained from (Adler et al., 2001; Wenzhöfer et al., 2001) or at http://www.geochemie.uni-bremen.de). The processes, which were considered for all model-runs shown below, comprise sediment advection, molecular diffusion, and 0th order kinetics of geochemical reactions. Diffusion coefficients were corrected for tortuosity (Boudreau, 1997) and a temperature of 2°C. For any given reaction, e.g., AOM, 0th order kinetics are calculated by defining maximum rates (R_{max}) for the reaction in question. The reaction-specific change in concentration at a specific depth ($\Delta C_{s,d}$) is then calculated by

$$\Delta C_{s,d} = R_{s,d} \times dt_{num} \times SC_{s,d} \quad (1)$$

where $R_{s,d}$ is the reaction rate in (mol L^{-1} yr^{-1}), dt_{num} is the time step used in the specific model run, and $SC_{s,d}$ is a stoichiometric factor. These rates (R_{max}) are used as long as they can be fulfilled by the available amount of the reactants. If a species is not available in sufficient amounts the rate is decreased automatically to avoid negative concentrations (Adler et al., 2001). All rates (R_i) given in the sections below refer to those "used" rates. The availability of each species in a potential reaction zone is then constrained only by the transport (diffusion or sediment advection) and its concentration at the upper and lower model boundary. Due to a generally observed overlap of SO_4 and CH_4 the maximum rates for this reaction (R_{SO_4}-CH_4) were set to 8×10^{-4} mol L^{-1} yr^{-1} (unlimited rates prevent any overlap of both species). The upper boundary condition is defined by bottom water conditions, which is the same for the major parameters SO_4 (28 mmol L^{-1}) and CH_4 (0 mmol L^{-1}) in all model runs. The lower boundary is generally defined as an open/transmissive boundary in all model runs presented below. This means that for any dissolved species the gradient of the last two cells is extrapolated to allow diffusion across the boundary. For CH_4 we used the specific option to define a fixed concentration at the lower boundary in specific model runs. Setting or changing the concentration of CH_4 at the lower boundary imposes varying diffusive fluxes and reaction rates of SO_4 and CH_4 in the model area. More specific details concerning the parameterization and data handling are given in the respective section below.

3. RESULTS AND DISCUSSION

3.1. Downslope Transport: Evidence from Digital Sediment Echosounder Data

To illustrate the type and the extent of sedimentary structures and phenomena originating from downslope transport that can be found in the studied area we show two PARASOUND sections recorded adjacently to the locations GeoB 2806 and 2809 (Fig. 2). Figure 2a shows a cross section of the continental slope between 3425 and 3650 m water depth directly crossing the location of GeoB 2806 (marked by a bar). The section upslope of 3600 m is characterized by parallel strong reflectors intercalated by transparent layers and lenses partly onlapping a strong reflector. Downslope of 3600 m, this reflector reaches the seafloor, becomes hummocky and is partly draped by acoustically transparent sediments. Below this strong reflector, no structures can be identified over the whole profile. A hummocky seafloor without subbottom reflectors can typically be referred to as a surface of large debris-flow deposits compressed by downward moving (Lee et al., 1999; Wynn et al., 2000), therefore this reflector is probably the surface of a large debrite. However, a second possibility is that the absorption of sounding energy is caused by gas. Both hypotheses can only be tested with multi-channel seismic data (deeper penetration than the Parasound System), which are unavailable. The non-deposition of hemipelagic sediments below 3600 m water depth is probably the result of bottom currents. The whole sediment package can be interpreted as a mix of hemipelagic sediments, and mass-flow deposits (i.e., slumps). The close-up shows a higher resolution of the sediment structures using a flattened sea floor projection at the core location. It clearly reveals an erosional contact at ~10 m and some strong reflectors above, which can be traced by other core data (see section 3.5).

The second cross section covers a slightly larger area to the northeast close to GeoB 2809 (Fig. 2b). Two hundred meters below the station, at a water depth of 3800 m, a similar transition from sediments characterized by parallel strong reflectors intercalated by transparent layers and lenses to a hummocky surface without penetration of sounding energy is visible (close-up in Fig. 2b). This sediment package can also be interpreted as a package of hemipelagic sediments and mass-flow deposits with a somewhat smoother transition to the hummocky seafloor compared to the profile in Figure 2a. The strong seafloor reflector below 3800 m water depth again suggests non-deposition or winnowing of fine-grained sediments due to bottom currents. A very prominent structure can be observed further up-slope between 3100–3200 m water depth where a large transparent unit settled on a sedimentary unit consisting of parallel reflectors (close-up in Fig. 2b). The surface of the upper part of this transparent body is also hummocky. Obviously, a slump was deposited on top of another package of hemipelagic sediments and mass-flow deposits. The hummocky surface (sensu Lee et al., 1999) is probably the result of deceleration of the slump due to changes of the preexisting seafloor gradient.

Both images give clear evidence for a very complex sedimentary environment dominated by gravity-driven downslope mass movements on different scales and influenced by bottom currents, creating the geochemical conditions as they are observed in the pore-water and solid phase as shown below.

3.2. Pore-Water Profiles of SO_4 and CH_4

All stations where SO_4 pore-water profiles were obtained are summarized in Table 1 along with the water depth of the station, the SO_4 penetration depth and the actual diffusive flux of SO_4 (and CH_4) into the transition zone (SMT). In some cases the SO_4 penetration depth had to be estimated since it was not reached within the cored sediment depth. A SO_4 penetration depth of more than 30 m may seem somewhat arbitrary with respect to the differing profile shapes (see below), but this procedure is helpful to obtain a quantitative relationship between all sampling sites (section 3.6).

Pore-water profiles of SO_4 show a large variety of shapes over the whole investigated area. The major types are summarized in Figure 3. In cores GeoB 6214, 6219, and 6223 (Figs. 3a–c) also CH_4 could be determined (no CH_4 data are available from the older cruise M 29-2) suggesting a net reaction of SO_4 and CH_4 as described by Niewöhner et al. (1998). Due to the fact that CH_4 is highly volatile under atmospheric conditions, most of the CH_4 present in situ had been escaped during core recovery and decompression. Whereas only traces of CH_4 could be detected at GeoB 6214, the other profiles show a sharp increase directly below the SO_4-CH_4 transition (SMT) and a scatter at greater depths indicating equilibration with atmospheric pressure. At those stations, where H_2S was determined the concentration profiles typically display a peak at the CH_4-SO_4 interface, while the peak area is correlated to the concentration of H_2S: the narrower the peak area, the lower is the concentration. Although some of the H_2S, which was originally dissolved in the pore-water, had possibly the same fate as most of the CH_4 this finding is consistent and will be addressed in section 3.5.

A very typical pattern that can also be deduced from Figures 3a–c (Transect I) is that the depth of the SO_4-CH_4 interface of ~4–5 m does obviously not change with water depth. This is consistent with estimates of the SO_4 penetration depth compiled in Table 1 and with measurements at the sediment-water interface (Hensen et al., 2000), which prove that intense mineralization processes are de-coupled from any water depth relation.

3.3. Transient Pore-Water Conditions

Apart from the so-called s-type (see section 3.4), all types of profiles shown in Figure 3 are already known from other studies (Borowski et al., 1997, 1999; Haese et al., 1997; Niewöhner et al., 1998; Pruysers, 1998) where a number of different explanations have been offered for almost the same phenomena. As a common explanation for the kink-type profile (see section 3.4) the re-oxidation of H_2S via Fe(III)-hydroxides was favored (Schulz et al., 1994), in spite of the lack of sufficient reactive Fe(III)-hydroxides (Haese et al., 1997). Nonlocal mixing by tube dwelling organisms or CH_4 bubble ebullition was suggested by Fossing et al. (2000). Their interpretation, however, lacks clear evidence for organisms pumping down the bottom water into the sediment (Zabel and Schulz, 2001) and there is no evidence for gas seeps in the region. Pruysers (1998) favored variations of the CH_4 flux from below (see below) disregarding, however, the effect of diffusion in his schematic model concept. Most concave down types are usu-

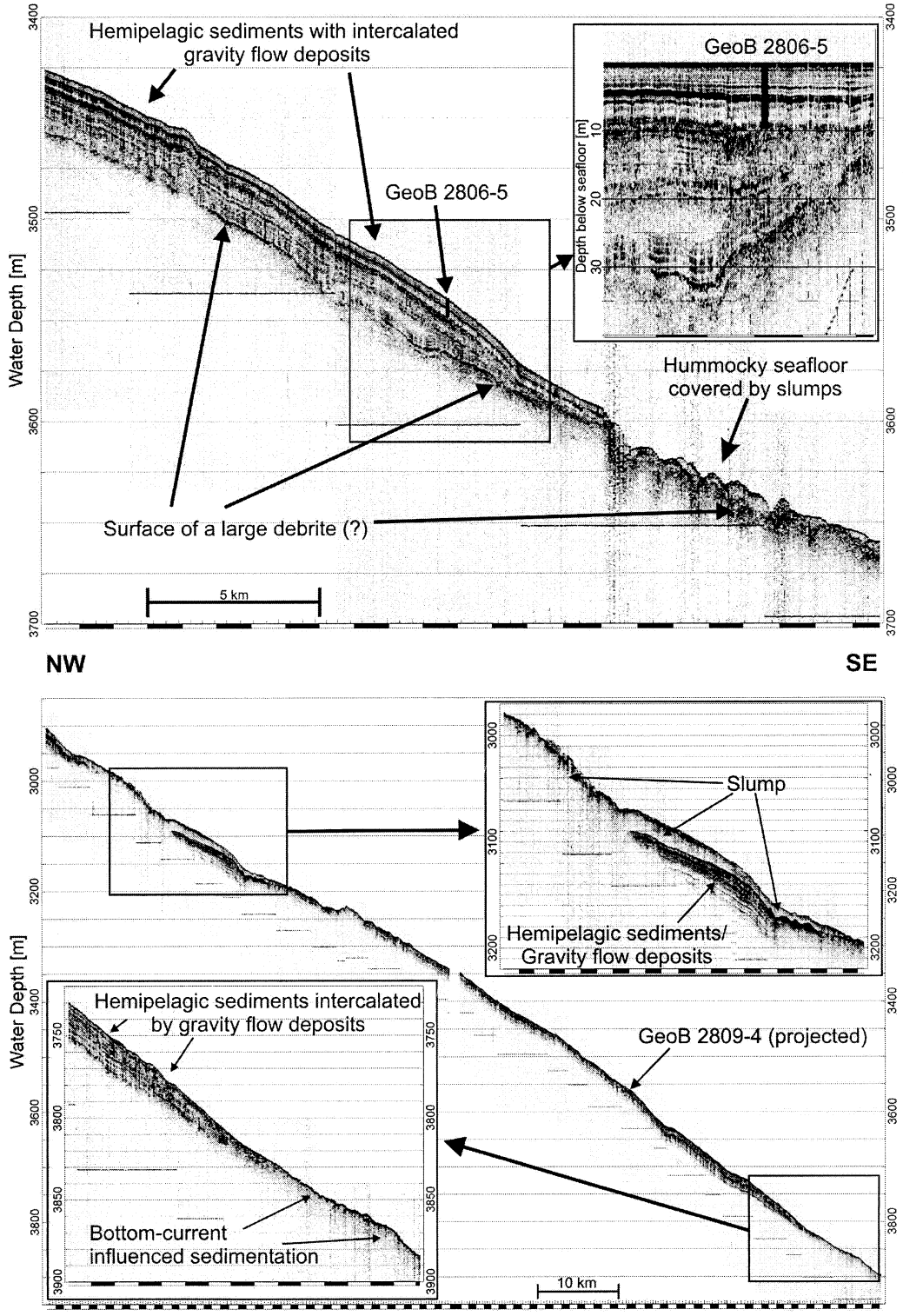

Fig. 2. Two PARASOUND sections from *MeteorCruise* M29/2 (Bleil and participants, 1994) crossing the continental slope in NW-SE direction. The figures were scaled from two-way travel time to depth for a constant sound velocity of 1500 m/s. (a) PARASOUND data from the vicinity of station GeoB 2806-5 (marked by a bar), which is located in a sediment package consisting of hemipelagic mass-flow deposits intercalated by small slumps. The hummocky seafloor suggests the surface of a large debris-flow deposit. The close-up shows a high-resolution, flattened sea floor projection of the direct surrounding of GeoB 2806 (discussed in section 3.5). (b) PARASOUND data from the vicinity of station GeoB 2809-4 imagining the complexity of sedimentation over a length of ~100 km. Close-ups showing a distinct slump (top) and the thinning of hemipelagic sediments and mass-flow deposits downslope, probably caused by bottom currents (bottom).

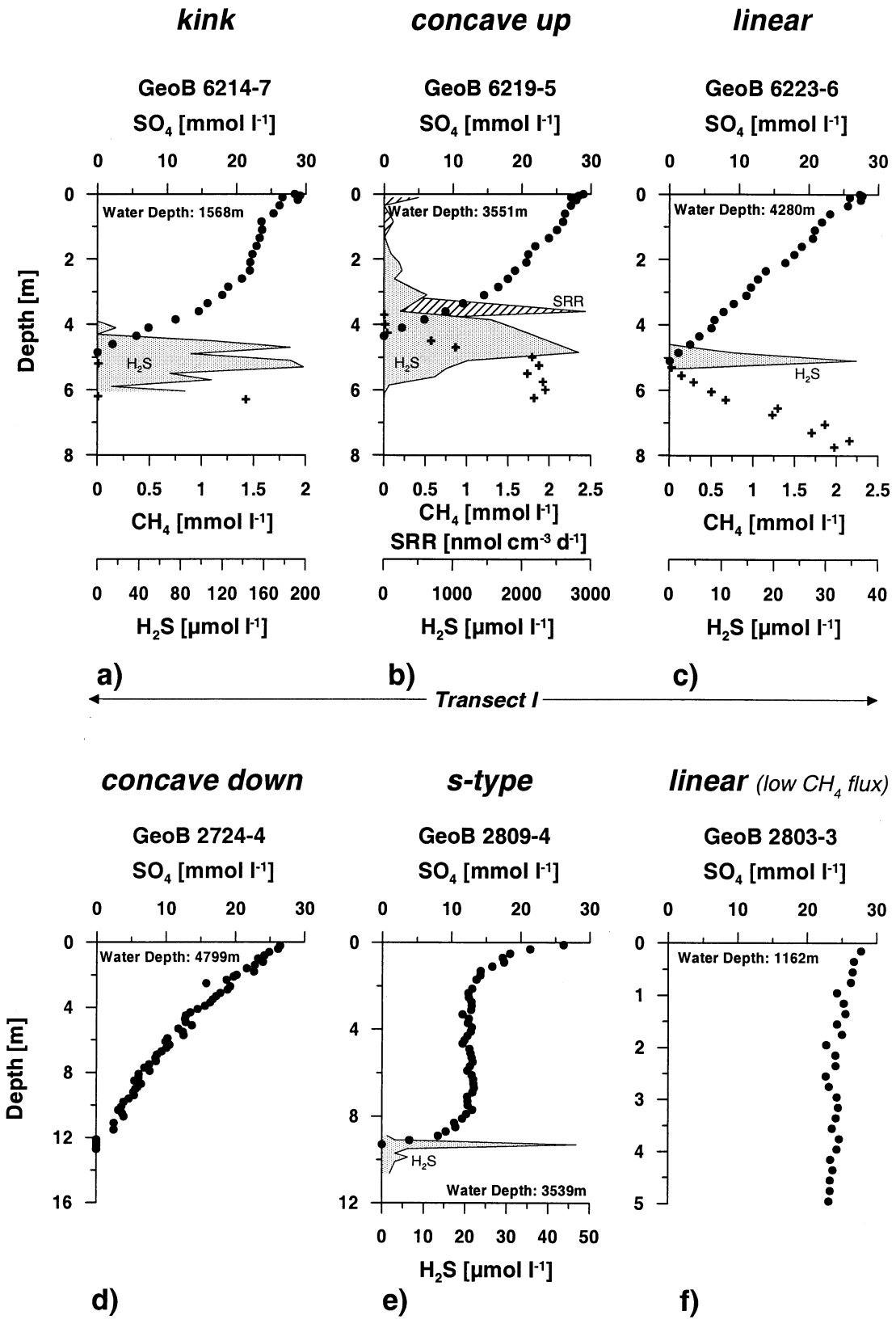

Fig. 3. Pore-water concentration profiles of SO_4 (dots), CH_4 (crosses), and H_2S (shaded) of six gravity cores. Sulfate reduction rates (SRR) were determined additionally at GeoB 6219-5. The headline of each graph describes the corresponding type of SO_4 profile. The cores displayed in (a–c) are perpendicular to the continental slope and marked as Transect I in Figure 1.

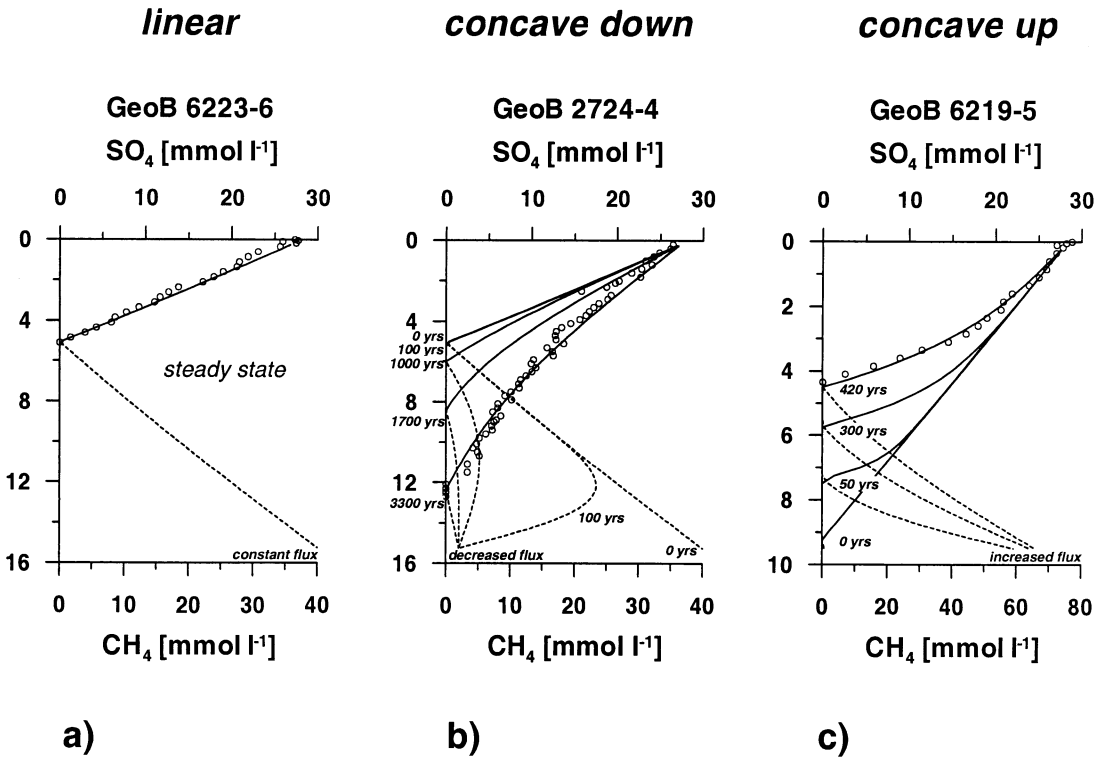

Fig. 4. Model results demonstrating the effect of decreasing and increasing CH_4 fluxes from deeper strata to simulate the concave down and concave up types. (a) Linear, steady state situation (used as starting condition for simulation for the concave down simulation); The maximum reaction rate of AOM within the SMT is R_{SO_4}-$CH_4 = 2.1 \times 10^{-4}$ mol L^{-1} yr^{-1}. (b) The present day concave down situation at GeoB 2724 is reached after more than 3000 yr when the CH_4 flux from below ceases (2 mmol L^{-1} at the lower boundary). R_{SO_4}-CH_4 decreases to $\sim 3.1 \times 10^{-5}$ mol L^{-1} yr^{-1} (c) Increasing the CH_4 flux from below produces the observed concave up situation at GeoB 6219 after 420 yr. R_{SO_4}-CH_4 increase from 1.2×10^{-4} mol L^{-1} yr^{-1} to R_{SO_4}-$CH_4 = 5.7 \times 10^{-4}$ mol L^{-1} yr^{-1} over simulation time.

ally attributed to continuous SO_4 reduction by organic matter degradation over depth (Borowski et al., 1999), which is a likely explanation. However, SRR determined at GeoB 6219 (Fig. 3b) and at comparable sites off Southwest Africa (Ferdelman et al., 1999; Fossing et al., 2000) indicate a de-coupling of high SRR driven by organic matter degradation at the sediment surface and AOM at greater depth. SRR in between both zones seem to be too low to significantly decrease sulfate in pore-water.

The major shortcoming of all of these hypotheses may be that they are based on the steady-state premise of pore-water conditions. Zabel and Schulz (2001) could demonstrate that a kink-type profile can be the result of a single slide event as long as the original pore-water signal is preserved in the sediment, a process that has already been described in a different context from sediments of the southern Norwegian Sea (De Lange, 1983).

As we will demonstrate below and in the following sections, most of the SO_4 profiles shown in this study are indicative for changes in the depositional conditions and thus reflect a transient stage. Only the linear type (Fig. 3c) truly reflects a present-day steady state situation of the pore-water SO_4 and CH_4 fluxes in a diffusion-controlled system. Concave up and down types may, however, be explained by changes in the CH_4 flux from below. A simple model study considering diffusive transport and anaerobic CH_4 oxidation can demonstrate this (Fig. 4). For the steady state situation shown in Figure 3c, a CH_4 concentration of 40 mmol L^{-1} is required at a sediment depth of 15 m, which is set as a fixed lower boundary concentration of CH_4 at this depth (Fig. 4a). Taking this as an arbitrary starting position for GeoB 2724 a decrease to $\sim$2 mmol L^{-1} CH_4 at this depth would produce approximately the observed SO_4 profile after 3300 yr (Fig. 4b). For a better illustration, a number of different time steps show the development of the concentration profiles over time. For the starting conditions of the scenario at GeoB 6219 the uppermost three SO_4-values were extrapolated by a linear gradient to a depth of $\sim$14 m. A sudden increase of the CH_4 concentration to $\sim$70 mmol L^{-1} (approximate concentration of dissolved CH_4 in equilibrium for gas hydrate formation at the given pressure/temperature conditions; Egeberg and Dickens, 1999) reveals the observed SO_4 concentration profile after $\sim$400 yr (Fig. 4c).

Although the starting conditions for such scenarios must be arbitrary, since the real changes in the CH_4 flux and their persistence over time are not known, it is a fully comprehensive explanation for the observed types of profiles. Thus, the major intention of performing these scenarios is to emphasize that these profiles most likely reflect transient states of the geochemical situation in the sedimentary pore-water system, indicative for changes on a timescale in the order of some

hundreds to thousands of years (Kasten et al., in press). Both scenarios in Figures 4b and 4c are based on drastic changes in the CH_4 concentration, for which an effective control mechanism is needed. Realistic mechanisms to fix or release CH_4 very fast are the formation or destabilization of gas hydrates. Due to pressure and temperature conditions at these water depths the formation of gas hydrates is generally favorable. Formation or destabilization would then depend on a sufficient, but potentially varying supply of CH_4 being produced below. Destabilization of gas hydrates may also add a slow advective component to the CH_4 flow. Although gas hydrates were not found, high CH_4 concentrations and AOM within the upper few meters of the sediments do suggest their existence. Additionally, CH_4 gas and gas hydrate findings at sediment depths between 10–30 m are reported from the central Argentine Basin (Manley and Flood, 1989).

However, significant variations in the flux of CH_4 are a possible, but not a necessary mechanism since both types of profiles can also reflect transient states after sedimentary events occurred. The concave up profile may also evolve from a kink-type profile as demonstrated below (section 3.4). In contrast, concave down profiles may develop as a result of erosion events. In case of such an event the top part of the sediment column and, thus, also of the sulfate profile would be removed. The re-equilibration of the system via diffusion of bottom water sulfate into the sediment could generate a similar profile as shown in Figure 4b. Whatever scenario is more likely, it is clear that the observed profiles reflect non-steady-state conditions in a dynamic sedimentary environment.

3.4. Kink and S-Type Profiles of SO_4: Recent Sedimentary Events

The types displayed in Figures 3a and 3e cannot be explained by changes in the CH_4 flux from below alone. As stated above, it could recently be shown that sedimentary slides "over thrusting" the sediments downslope are the most likely reason for the "kink" type (Zabel and Schulz, 2001). Thus, the observed situation displays another category of transient pore-water state.

3.4.1. Kink-Type

In Figure 3a we can observe a very sharp kink in the SO_4 concentration profile at ~2.80 m. To create such a pore-water profile the prerequisite is that both sediment sections had different SO_4 gradients when sliding on top of each other. The SO_4 gradient of the upper part was probably formed in a sediment sequence with a weak SO_4 gradient on the upper part of the slope and cut off at about this depth when sliding downslope. Indeed, there is such evidence coming from the observation at core GeoB 2803, located upslope at a water depth of 1162 m (Fig. 3f). The SO_4 profile at this station decreases only by a few mmol L^{-1} within the upper 5 m. Deeper penetration of SO_4 in upper slope sediments is the result of reduced rates of CH_4 formation caused by prevailing erosion and winnowing of fine-grained organic material (see section 2.1). This is further indicated by decreased SO_4 fluxes (downward movement of the zone of AOM) towards the shelf (Table 1).

Since the gradients have not significantly smoothed over time due to diffusion, it is likely to assume that the event at site

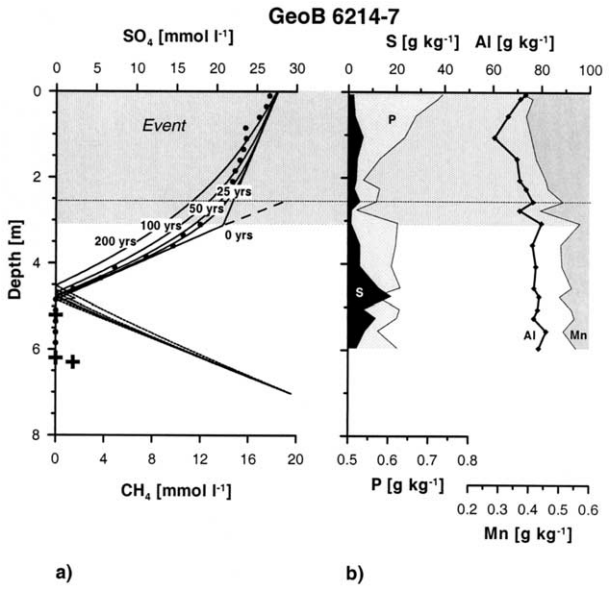

Fig. 5. (a) Development of the SO_4 pore-water profile at site GeoB 6214 with constant CH_4 flux from below after a slide was deposited. Starting with two different, original SO_4 gradients in the "event-section" and the sediment below (marked by 0 yr) the diffusion-controlled changes of the SO_4 pore-water profile are displayed for the next 200 yr. Most likely, the sedimentary slide occurred less than 50 yr ago. Extrapolating the SO_4 gradient of the underlying sediments to an imaginary original sediment surface (bottom water concentrations 28 mmol L^{-1}) allows a rough estimation of the thickness of the eroded surface sediment section. Maximum rates of R_{SO_4}-CH_4 of 8×10^{-4} mol L^{-1} yr^{-1} are reached in this scenario and do not vary significantly due to similar gradients within the observed time span. (b) The supposed slide plain is indicated by sharp transitions in the solid phase profiles of aluminum, phosphate, and manganese. The SMT is characterized by a distinct sulfide enrichment.

GeoB 6214 has probably occurred very recently. Figure 5a shows a scenario with two very sharp SO_4 gradients, which characterize the initial situation, and a CH_4 profile, which is approximately in steady state with the lower SO_4 gradient. AOM has been simulated according to Eqn. 2 where imposed maximum rates of R_{SO_4}-CH_4 of 0.8 mmol L^{-1} yr^{-1} were reached. After a time period of 25–50 yr diffusion has smoothed the shape of the profile such that the observed profiles can be convincingly represented. Another 50–150 yr later diffusion would have further smoothed the shapes and due to the lower SO_4 gradient the SMT would have moved slightly upward (constant CH_4 concentration at the lower boundary). Thus, we can estimate that the sliding event took place not more than 50 yr ago. Moreover, the significant enrichment in sedimentary sulfur at ~5 m depth (Fig. 5b) indicates that the zone of AOM has probably not shifted significantly for a longer period of time (see discussion in section 3.5).

However, two more interesting results can be obtained from this scenario: (1) Extrapolating the lower SO_4 gradient from ~3.1 m (starting conditions) linearly until bottom water concentrations are reached, the original sediment surface would have been at a sediment depth of now 2.5 m, which means that ~0.6 m have been eroded by the sliding event. Even though this is only a crude approximation it gives an idea of the magnitude of the mass (re-) movements. (2) As already men-

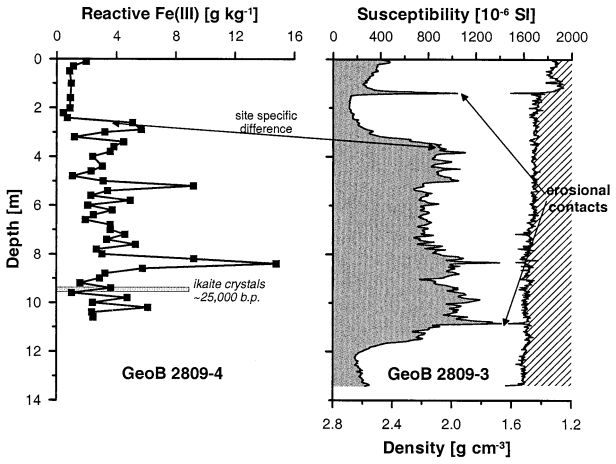

Fig. 6. Reactive Fe(III), susceptibility, and density profiles at site GeoB 2809. The increase of reactive Fe(III) concentrations are in line with the increase in susceptibility below 2–3 m (note that the cores a different in length and the sedimentary sections are slightly shifted). Two erosional contacts are known from visual core description (Bleil and participants, 1994) and are marked by distinct peaks in density and susceptibility. Ikaite crystals occur at a depth of 9.40 m.

tioned above, after some hundreds of years of diffusion a concave up shape of the SO_4 profile will establish from the kink-type.

The idea of a slide event is further supported by solid phase analysis. Concentration profiles of aluminum, phosphate and manganese show distinct, sharp transitions indicating a drastic change in sediment composition at the depth of the suggested slide plain (Fig. 5b).

3.4.2. S-Type

To gain a logical and physically possible explanation for the s-type profile obtained from site GeoB 2809 (Fig. 3e) needs, however, a more demanding approach. A steady state explanation in this case would require a process that consumes SO_4 to a depth of nearly 2 m, using up exactly such an amount of SO_4 that diffusion from the overlying bottom water is able to "equilibrate" the system at about half of the SO_4 seawater concentration in the pore-water. Furthermore, SO_4 reduction must not occur between 2 and 8 m, but at 8 m depth an additional SO_4 source would be required to maintain the concentration of $\sim$13 mmol L^{-1} with regard to the SO_4 consumption within the SMT. In Figure 6 additional information from solid phase geochemical analyses and physical properties is shown. The most prominent feature in this core are the very high reactive Fe(III) concentrations between 2.6 and 10.6 m sediment depth (determined by ascorbate and dithionite extractions) with up to 15 g kg^{-1} and an average value of $\sim$4 g kg^{-1}, which are as high as the concentrations in surface sediments (Haese et al., 2000). The existence of a sediment sequence of 8 m thickness containing high amounts of reactive Fe(III) that have not already been reduced by diagenetic processes closer to the sediment surface (Hensen et al., 2000) suggests that the sedimentation must have happened faster than diagenetic overprinting. Furthermore, the existence of this "massive" Fe(III) layer actually requires a thickening of the sedimentary strata, which might be explained by lateral compression due to the sliding or slumping of the sediments. The zone of elevated Fe(III) contents is also clearly reflected by the susceptibility signal (Fig. 6) measured at a parallel core at station GeoB 2809, which makes this phenomenon easy to trace. The onset of the higher susceptibility signal is, however, somewhat shifted compared to the Fe(III) signal, which can be attributed to the spatial heterogeneity because cores were not obtained exactly from the same site. Assuming that the high Fe(III) section represents a single slide, the deeper-reaching susceptibility signal of the longer parallel core indicates that the base of it is reached at a sediment depth of $\sim$11 m. Further evidence for this theory comes from the visual core description (Bleil and participants, 1994) where indications for erosional contacts are described at 1.4 and 11 m below the sediment surface, which are clearly marked by distinct peaks in sediment density (Fig. 6). Additionally, ikaite crystals were found at a sediment depth of 9.40 m, which have been dated to an age of $\sim$25 kyr (^{14}C AMS). Due to the limited supply of ^{14}C by diffusion (as shown by Zabel and Schulz, 2001, for a similar environment) it is unlikely that the crystals have originally grown at this sediment depth. Combining all these information, it is evident that at least two slides or sedimentary events occurred, establishing the present-day situation. As shown for the kink-type, the "re-moved" sediment packages may carry their geochemical signature from their origin, thus the accumulation of different packages with originally different pore-water signatures should be able to produce any type of pore-water profile, only forced by the position of the SMT and diffusion. A model scenario consistent with all observations is presented in Figure 7. The measured SO_4 profile is shown again in Figure 7a together with the alkalinity profile, which is nearly mirroring the SO_4 -profile and thus emphasizing that the pore-water profile is not an element-specific feature. In Figure 7b the starting conditions for the model scenario are shown, characterizing how the pore-water conditions were directly after the events had occurred. The SMT with a steep SO_4 gradient is located between 10–11 m (slightly correcting for the depth-shift between the two parallel cores), the CH_4 concentration at a depth of 12 m is arbitrarily chosen to be 30 mmol L^{-1} (lower boundary condition) and the bottom water SO_4 concentration is 28 mmol L^{-1} (upper boundary condition). Above the transition, the SO_4 concentration is almost constant with a certain scatter of data, however, we chose two slightly different gradients over depth to mark the possible differences due to differences in origin of the sediment sections. There is no strict constraint for the exact SO_4 concentrations between 2 and 8 m, but it is necessary that they match with the average measured concentrations. Within the SMT, SO_4 and CH_4 are allowed to react with maximum rates of 0.8 mmol L^{-1} yr^{-1}. The results of the simple transport-reaction model are shown after 8, 25, 250, and 500 yr (Fig. 7c). The 25 yr simulation provided an optimal fit to the data. This short period of time is supported by the solid phase observations. A longer persistence of the AOM at this depth would have caused a significant reduction of reactive Fe(III) concentrations and a drop in the susceptibility signal (see section 3.5). It is evident that diffusion is very effective in smoothing the concentration differences on short scales. After a few hundreds of years—in this case with a constant CH_4 flux—the original geochemical signature is wiped out by diffusion combined with

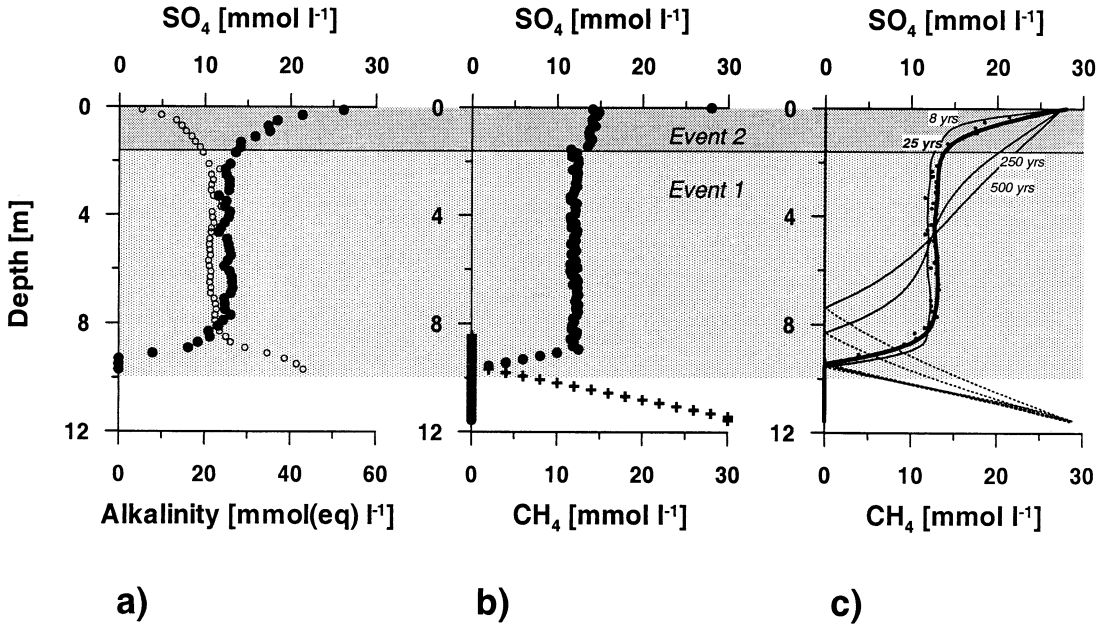

Fig. 7. Modeling the s-type SO_4 pore-water profile. (a) Measured pore-water profiles of SO_4 (filled dots) and alkalinity (open dots) emphasizing the non-state state situation. (b) Starting conditions for SO_4 and CH_4 after two events occurred. Slide sections are assumed to have different SO_4 gradients. Development of SO_4 and CH_4 pore-water profiles over time applying constant CH_4 concentration at greater depth. The observed SO_4 profile is reached after ~25 yr. Over time the original pore-water signature is wiped out. The SO_4 profile will turn into a slightly concave up/linear type accompanied by an upward movement of the SMT. Initial rates reach the maximum value of R_{SO_4}-CH_4 ($=8 \times 10^{-4}$ mol L^{-1} yr^{-1}) due to very steep gradients and decrease as the gradients smooth (2.4×10^{-4} mol L^{-1} yr^{-1}; 500 yr).

slight upward movement of the SMT, thus illustrating the transient nature of the geochemical conditions in these sediments.

It appears that both, kink- and s-type are obviously very short-lived phenomena that should make it difficult to trace them at all. Actually, the kink-type is a more ubiquitous feature as it is reported from a number of different sites (see above), but a closer look on the available data reveals that, in most cases, the kink is not very sharp so that probably a number of different transient states are represented. Furthermore, it must be considered that with increasing sediment depth, thus increasing distance from the sediment surface (or thickness of the slide section) and the SO_4 source, it will take longer to wipe out the traces of the sedimentary event. Due to the very special conditions required for the s-type profile and its short-lived nature, it can be expected that this type is much less ubiquitous and a search for it should be more like looking for the needle in a haystack. However, to our knowledge, this is the first profile of this kind published emphasizing the hypotheses above.

3.5. Reconstruction of Sedimentary Events on Longer Time Scales

On longer timescales pore-water concentrations equilibrate towards a new steady state, thus, a detailed analysis of solid phase information is required to trace back the sedimentary history. In Figure 3c a linear SO_4 profile is shown for GeoB 6223 suggesting steady state pore-water conditions. A similar profile was obtained at GeoB 2806, which is plotted together with the H_2S, Fe^{2+}, and PO_4 pore-water profiles in Figure 8a. The SMT is located at nearly 4 m forming a broad sulfidic zone with two redox fronts between 3 and 6 m. Concentrations of dissolved iron are generally below 10 μmol L^{-1} and the profile does not show any conspicuous sinks and sources, thus there are no indications for bacterial iron reduction in the pore-water record. The phosphate concentrations increase linearly with increasing depth, showing a maximum at ~6 m and a marked drop below. This drop in phosphate coincides with an increase in reactive Fe(III) minerals and susceptibility (Fig. 8b). The amount of Fe(III) minerals (up to 6 g kg^{-1}) is comparable to those concentrations at GeoB 2809. Fe(III) minerals usually have a high binding-capacity for dissolved phosphate (Mach et al., 1987; Güchter et al., 1988; Lucotte et al., 1994; Föllmi, 1996), thus, it is suitable to explain the observed drop in PO_4 concentrations. Since this horizon marks the lower zone of H_2S fixation, the most likely process occurring at this redox front is the dissolution of Fe(III)-minerals by H_2S with a simultaneous release of previously bound phosphate.

The massive occurrence of reactive Fe(III) minerals can, according to GeoB 2809 (Fig. 6), be attributed to a sedimentary slide or slump (Event 1) and a fast burial to prevent an earlier reduction within the diagenetic sequence. Further evidence for sedimentary slides comes from the density profile, which shows a marked positive shift at ~3 m and a reversed trend below down to a depth of 4 m, where another prominent shift can be observed (Fig. 8b). This observation, pointing to abrupt changes in the lithological complex, is supported by the echosounder data as shown in the close-up of Figure 2a, since the succession of reflectors can be related to the subdivision of events as suggested in Figure 8. Additionally, the reflector at

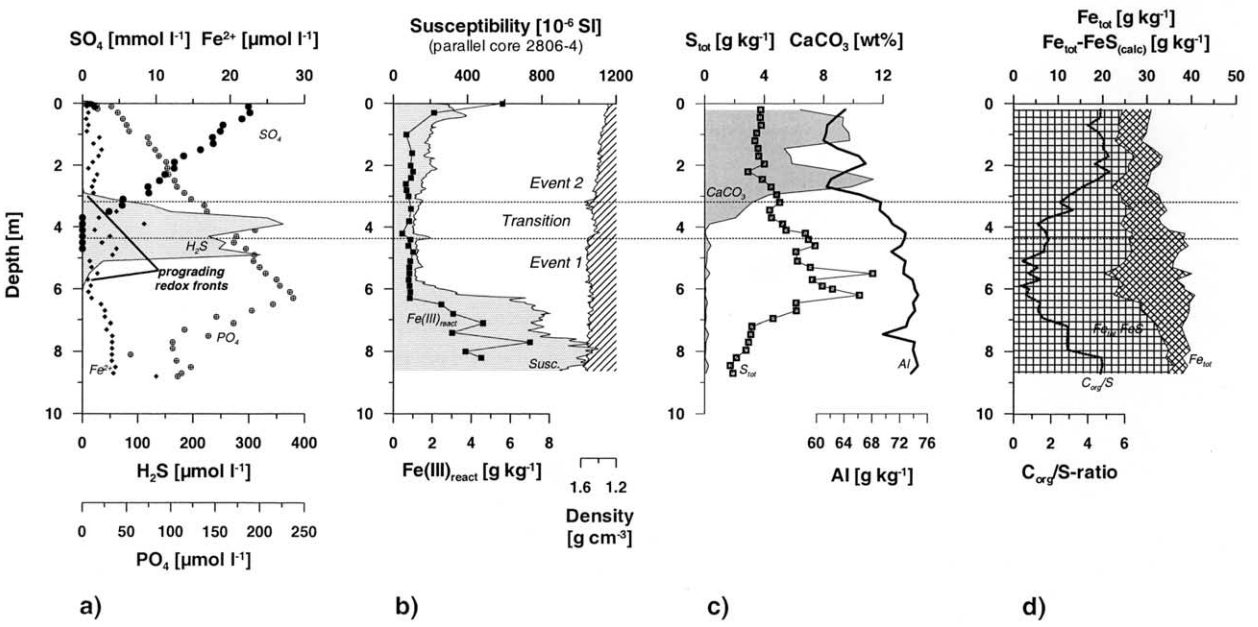

Fig. 8. Geochemical and physical properties data at site GeoB 2806. (a) The almost linear SO_4 pore-water profile suggests steady state conditions, whereas the H_2S profile indicates two active redox fronts (the lower one accompanied by significant drop in PO_4) indicating non-steady state conditions. (b–d) Solid phase and physical properties data support the existence of at least 2–3 sedimentary events (see also close-up of Fig. 2a). $FeS_{(calc)}$ is calculated from S_{tot} by the simplified assumption of an 1:1 stoichiometry (no pyrite). See text for more details.

~10 m marking an erosional contact is probably indicative for the lower limit of Event 1 and, thus, marks its vertical extensions. The transitional section (3–4 m) is accompanied by a distinct change in mineralogy, where the $CaCO_3$ content abruptly drops from ~10 wt% to nearly 0 wt%. This is accompanied by a shift in the aluminum content, clearly documenting different sources of the sediment sections with varying amounts of biogenic and terrestrial fractions (Fig. 8c). These observations point to the existence of at least two sedimentary slide sections with a broad transition zone or a thinner third one in between.

A simple shift in sediment composition instead of a sudden emplacement of the sedimentary succession above 4 m would not be in agreement with the observed data. Normal marine sedimentation after Event 1 (assuming a sedimentation rate between 5–10 cm kyr^{-1}; Ewing et al., 1971) implies 40,000–80,000 kyr to build up the upper 4 m. This rate of sediment accumulation would not have been high enough to compensate for the CH_4 flux from below and stabilize the zone of AOM at a depth between 4 and 6 m. That this zone has not been shifted significantly over time can be deduced from the total sulfur (S_{tot}) profile, which shows a prominent enrichment at this depth and low, almost constant values at the top and the base of the core (Fig. 8c). The C_{org}/S-ratio (Fig. 8d) is similarly depleted to values between 0.4–1.9 (global average for anoxic sediments is 2.8–3; Berner, 1982; Berner and Canfield, 1989). The process of AOM enriches allochthonous sulfur from SO_4 and it depletes the original C_{org}/S-ratio, thus, a primary source for the sulfur enrichment can merely be excluded. Calculating the maximum content of FeS from S_{tot} (with the simplifying assumption that there is no sulfur bound to pyrite and other sulfides) and subtracting this amount from the total Fe-content (Fe_{tot}), the difference of both marks the zone of sulfide precipitation even clearer (Fig. 8d).

Postdepositional enrichments of iron sulfides have been reported many times in literature and generally related to non-steady state diagenesis. The rapid decrease in Holocene sedimentation rates were identified to have caused the fixation of the zone of AOM at a certain depth in Amazon Fan sediments leading to the formation of distinct peaks of iron sulfides within the last 10000 yr (Kasten et al., 1998; Adler et al., 2000). Similarly, diagenetic pyritization due to changes from aerobic to anaerobic sedimentary conditions are a widespread feature that occurred during cyclic formation of sapropels in the eastern Mediterranean Sea (Passier et al., 1996, 1999). High subsurface SRR during sapropel-formation in combination with Fe-limitation induced a downward migration of H_2S and subsequent reaction with Fe^{2+} that was mobilized from iron (hydr-) oxides, partly formed above earlier oxidation fronts (Passier et al., 1996). Accordingly, the central idea for our model approach is that after deposition of the slides a Fe(III)-H_2S redox-horizon was formed forced by H_2S production within an almost stationary zone of AOM. As soon as the reactive Fe(III) minerals ($Fe(III)_{react}$) were consumed directly within this horizon, H_2S started to diffusive upwards and downwards, thus forming slowly prograding redox fronts presently marked by the upper and the lower limit of dissolved H_2S (Fig. 8a).

The major approach to calculate the time elapsed since the sedimentary events occurred encompasses the central question, for how long SO_4 reduction and FeS precipitation have lasted. To develop a reasonable model scenario, it is crucial to know how much reactive iron has been converted and by which rate. It is reasonable to assume that the whole section of Event 1 (below 4 m) had originally the same average concentration of

Table 2. CH_4 concentrations at the lower boundary ($CH_{4\text{-}LB}$), maximum reaction rates, and the sum of reaction rates for Eqns. 2–4 are listed for the model scenario at site GeoB 2806 as shown in Figure 9.[a]

	Time intervals							
Parameter	Start (20)	0–800	800–1600	1600–2400	2400–3200	3200–3800	3800–4000	End 4050
$CH_{4\text{-}LB}$	12	12	16	20	24	30	36	*36*
$R_{SO4\text{-}CH4}$								
Max	5.9×10^{-4}	5.9×10^{-4}	8.0×10^{-4}	8×10^{-4}	8×10^{-4}	8×10^{-4}	8×10^{-4}	*8×10^{-4}*
Sum	9.5×10^{-4}	9.5×10^{-4}	1.1×10^{-3}	1.2×10^{-3}	1.3×10^{-3}	1.5×10^{-3}	1.6×10^{-3}	*1.6×10^{-3}*
$R_{Fe(III)react}$								
Max	4.0×10^{-5}	4.0×10^{-5}	4.0×10^{-5}	4.5×10^{-5}	5.5×10^{-5}	7.0×10^{-5}	1.2×10^{-4}	*9.5×10^{-6}*
Sum	3.0×10^{-4}	3.0×10^{-4}	3.3×10^{-4}	3.7×10^{-4}	3.7×10^{-4}	4.0×10^{-4}	2.5×10^{-4}	*9.6×10^{-6}*
$F_{Fe(III)relict}$								
Max	1.3×10^{-6}	1.3×10^{-6}	1.7×10^{-6}	2.3×10^{-6}	3.3×10^{-6}	2.7×10^{-6}	2.0×10^{-5}	*3×10^{-5}*
Sum	1.6×10^{-6}	1.6×10^{-5}	2.7×10^{-5}	4.8×10^{-5}	7.5×10^{-5}	7.1×10^{-5}	2.7×10^{-4}	*4×10^{-4}*
R_{FeS}								
Max	8.3×10^{-5}	8.3×10^{-5}	1.0×10^{-4}	9.5×10^{-5}	1.4×10^{-4}	1.7×10^{-4}	2.8×10^{-4}	*6.4×10^{-4}*
Sum	6.4×10^{-4}	6.4×10^{-4}	7.1×10^{-4}	8.3×10^{-4}	8.8×10^{-4}	9.3×10^{-4}	1.0×10^{-3}	*8.5×10^{-4}*

[a] Note that more time intervals are shown than displayed in Figure 9. $CH_{4\text{-}LB}$ is in mmol L^{-1} and reaction rates (R_i) are in mol L^{-1} yr^{-1}. Maximum rates of $R_{SO4\text{-}CH4}$ of 8×10^{-4} mol L^{-1} yr^{-1} are nearly always reached throughout the modeled time span. The reaction rates correspond to the end point of the given time step. The last column (italics) gives hypothetical reaction rates to maintain the observed H_2S profile when $Fe(III)_{react}$ is completely consumed within the SMT.

reactive Fe(III)-minerals as it can be found below 6 m. This is further supported by the FeS enrichment in relation to nearly unchanged amount of Fe_{tot} (Fig. 8d), suggesting precipitation of in situ available iron and no significant diffusive source of Fe^{2+} (Fig. 8a). Reaction kinetics of H_2S with a continuum of different Fe(III)-phases are the other crucial parameters to be resolved. We developed a simple approach for the estimation of reaction rates, based on empirical observations of H_2S and Fe^{2+} concentrations observed in sediments of this area (Figs. 3 and 8), and unpublished data from other GeoB cores available on the database Pangaea (at http://www.pangaea.de). Usually, the concentrations of H_2S are between a few tens to some hundreds of μmol L^{-1}, whereas dissolved Fe^{2+} concentrations are below 20 μmol L^{-1}. Additionally, the maximum H_2S-concentration reflects the availability of $Fe(III)_{react}$ since H_2S is e.g., much higher at GeoB 2806 compared to GeoB 2809 (Figs. 3 and 8). Considering the following reactions (Eqns. 2–4) as dominantly responsible for the fate of dissolved H_2S and Fe^{2+} we have sufficient constraints for a comprehensive description of the system.

$$CH_4 + SO_4^{-2} + H^+ \rightarrow HCO_3^- + H_2O + \mathbf{H_2S} \quad (2)$$

$$2Fe(OH)_3 + \mathbf{H_2S} \rightarrow 2Fe^{2+} + 2H_2O + 4OH^- + S^0 \quad (3)$$

$$Fe^{2+} + \mathbf{H_2S} + 2OH^- \rightarrow FeS + 2H_2O \quad (4)$$

The constraints are sufficient, because the amount of H_2S produced by AOM is determined by almost constant gradients of SO_4 and CH_4. Thus, only the reaction rates of Eqns. 3 and 4 have to be determined to obtain H_2S- and Fe^{2+} concentrations within the limits given above. Eqn. 3 is the most critical, since more effective, rate to determine: (a) A very low rate leaves much H_2S remaining in pore-water, because Fe^{2+} production is also low, provided that Eqn. 4 is the only, quantitatively important pathway to remove H_2S and Fe^{2+}. This would create much higher peaks than observed in the sediment. (b) If the rate is too high, relatively too much Fe^{2+} is produced, which cannot be consumed via Eqn. 4 since the required H_2S is already consumed via Eqn. 3 and thus, Fe^{2+} concentrations would increase.

To verify the hypotheses made above, we developed a model scenario that considered the dissolved species SO_4, CH_4, H_2S, and Fe^{2+}, the solid species $Fe(OH)_3$ (=$Fe(III)_{react}$ and $Fe(III)_{relict}$) and FeS as well as reaction rates for Eqns. 2–4. The second Fe(III)-phase ($Fe(III)_{relict}$) was invented to compensate for the background reactivity of all other Fe(III)-minerals (i.e., sheet silicates), which were not determined by the chemical leaching methods. This also includes the relict concentrations of $Fe(III)_{react}$ of ~0.8–1.0 g kg^{-1} (Fig. 8b), which are obviously a less reactive background amount of Fe(III) minerals determined by the leaching methods. The reaction rates and changes of the CH_4 concentration at the lower boundary ($CH_{4\text{-}LB}$) used for the model run are summarized in Table 2. The final result is presented in Figure 9, showing the development of concentration profiles of dissolved and solid phase species and reaction rates for some specific time marks. Anticipating the major outcome, we estimate that the time period, which is required to obtain present day conditions, is ~4000 yr. The recently measured profiles and starting concentrations are plotted in Figure 9a,b (first 2 graphs in each row). Concentrations of $Fe(III)_{react}$ were set to be 4 g kg^{-1} for the whole section of Event 1 including 0.8 g kg^{-1} of the aforementioned nonreactive amount of $Fe(III)_{react}$ (Fig. 8b). $Fe(III)_{relict}$ concentrations were estimated according to (Haese et al., 2000) to be at least half of the Fe_{tot}-FeS concentrations (on average 10 g kg^{-1}), thus being sufficiently available as shown in Figure 8. The FeS concentrations (derived from total sulfur concentrations; Fig. 8c) above and below the 3–6 m zone were taken as a background for the model runs. Although of minor importance, a continuous "background" sedimentation rate of 5 cm 1000 yr^{-1} was calculated for the time span after the events occurred.

The starting conditions for CH_4 and SO_4 were, for simplicity, defined as a steady state situation of both fluxes with an SMT at ~6 m. This may, strictly speaking, not be correct, but given by the depth of the C_{org}/S-depletion and the insensitivity

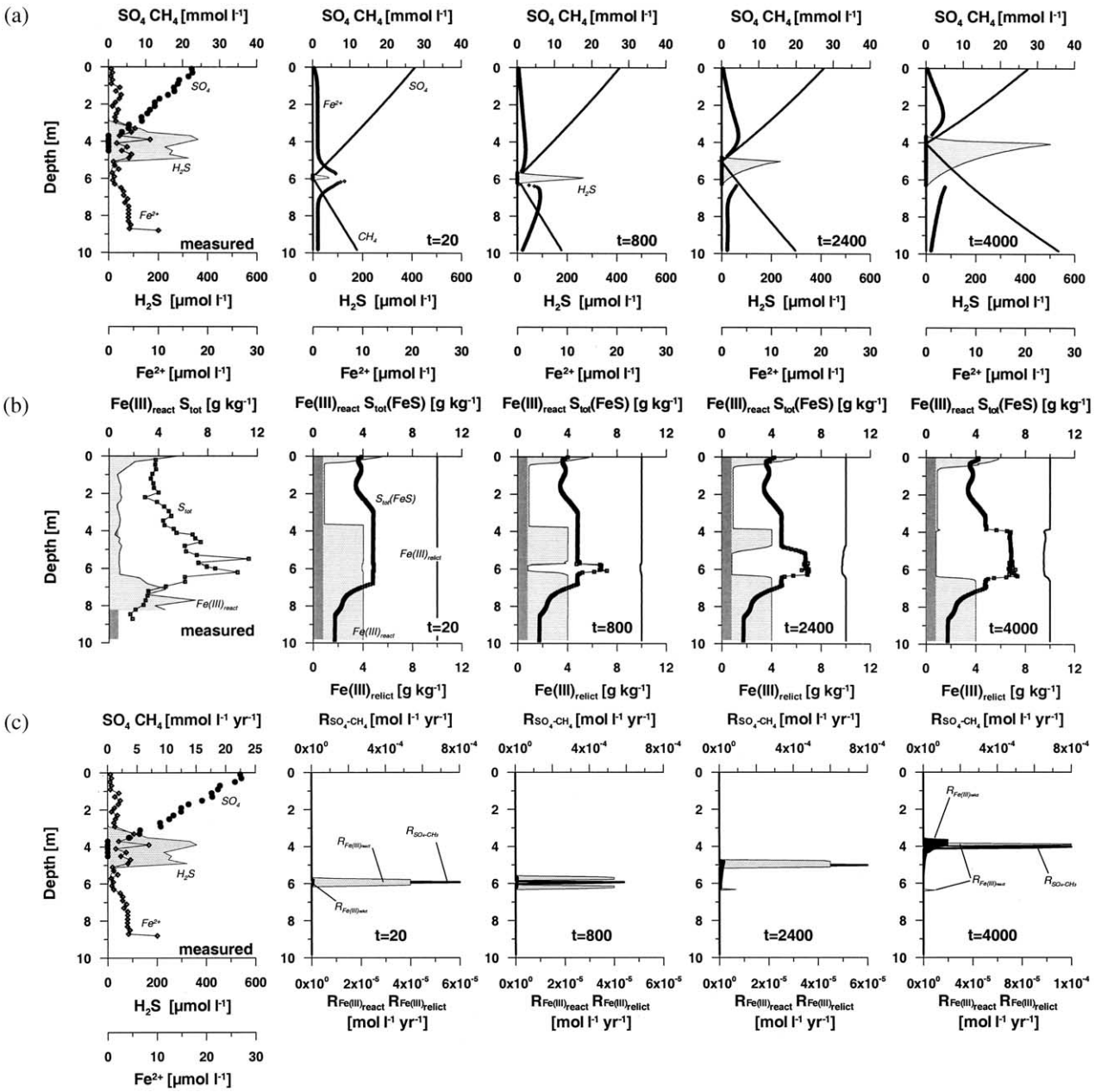

Fig. 9. Model scenario showing the development of the geochemical situation at site GeoB 2806. The first graph in each row shows the measured concentrations in pore-water and in solid phase. The following graphs in each row show the model output based on the redox processes listed in Eqns. 2–4 at selected time marks of 20 (=starting conditions), 800, and 2400 yr until the present day situation is reached (4000 yr). (a) Pore-water profiles of SO_4 (dots, solid line), CH_4 (solid line), Fe^{2+} (diamonds), and H_2S (shaded). (b) Solid phase profiles of $Fe(III)_{react}$ (shaded; background concentration darker), $S_{tot}(FeS)$ (total sulfur calculated from FeS precipitation; squares), and $Fe(III)_{relict}$ (solid line). (c) Reaction rates over depth R_{SO_4}-CH_4 (solid line), $R_{Fe(III)react}$ (shaded), $R_{Fe(III)relict}$ (filled black area). Sedimentation rate is 5 cm 1000 yr^{-1}. For changes of CH_4 at the lower boundary see Table 2.

of CH_4 and SO_4 profiles after a certain period of time (see section 3.3; Figs. 5 and 7c) it is a reasonable assumption. To comply with the fact that the major peak of S_{tot} and thus FeS is at ~6 m, it can be deduced that the position of the SMT has moved upward over time from ~6 m to the present day depth of 4 m (increase of the CH_4 concentration at the lower boundary in distinct steps as shown in Table 2). The upward movement of the SMT as it is still indicated by the slight concave up shape of the measured SO_4 profile (Figs. 8 and 9) could, however, still be due to the adjustment towards steady state conditions (as shown for the s-type scenario in Fig. 7c). Accordingly, steeper gradients with initially higher reaction rates could have occurred (cf. GeoB 2809; Fig. 7) compared to the scenario presented in Figure 9. Since the system levels out quite fast this would only be of minor importance for the general model result.

At the starting point a surplus of $Fe(III)_{react}$ was available at the depth of AOM, comparable to the present day situation at GeoB 2809 (Fig. 6). Thus, we adjusted the reaction rates for Eqns. 3 and 4 (mainly $R_{Fe(III)react}$ and R_{FeS}; Figure 9c and Table 2) by the requirement that resulting Fe^{2+} is low (<20 μmol L^{-1}) and H_2S is ~50 μmol L^{-1} for this steady state situation (Fig. 9c). By doing this, we found that the maximum rates ($R_{Fe(III)react} = 4–6 \times 10^{-5}$ mol L^{-1} yr^{-1} for the starting situation) are a highly sensitive factor. Already halving or doubling $R_{Fe(III)react}$ results in H_2S concentrations of either ~0 or >200 μmol L^{-1}, respectively. Decreasing or increasing the order of magnitude of $R_{Fe(III)react}$ leads to completely unrealistic results with large Fe^{2+} peaks and H_2S concentrations of several mmol L^{-1}. Reaction rates of H_2S with very reactive Fe(III) minerals (e.g., ferrihydrite, lepidocrocite) obtained from experimental studies are some orders of magnitude higher (1–5 mol L^{-1} yr^{-1}) than the rates used for the model study (see compilations of Canfield et al., 1992, or Thamdrup, 2000). Since those were often derived from experimental setups with synthetic minerals and stirred solutions they are not comparable to the deep marine environment, where exchange with the surrounding pore-water is limited by diffusion. Thamdrup (2000) reports that reaction rates of goethite and hematite (in the order of 1×10^{-3} to 1×10^{-1} mol L^{-1} yr^{-1}) are more typical for more reactive coastal sediments, which supports the reliability of the model-derived rates for deep-sea sediment.

As soon as $Fe(III)_{react}$ is used up within the zone of AOM, H_2S concentrations increase, because of the distance to the now developed reaction fronts above and below (Fig. 9a). The more the reaction fronts are moving apart from the SMT, thus broadening the zone with free H_2S, the higher is the raise in H_2S concentrations (see also Fig. 3b) reflecting the "aging" of the minerals. Due to the present day position of the SMT $R_{Fe(III)react}$ decreased over time at the lower redox front (Fig. 9c). This situation might, however, reversed as soon as $Fe(III)_{react}$ is completely consumed within upper sediment column accompanied by an overall increased H_2S levels in the pore-water. To compensate for these processes in the model run, the reaction rates were slightly increased over time (listed in detail in Table 2). The reasoning for this is as follows: (1) As the zone of AOM moves upward due to higher fluxes of SO_4 and CH_4, the H_2S production is increased by increased reaction rates (R_{SO_4}-CH_4; Eqn. 2), thus $R_{Fe(III)react}$ will also increase over time (Eqn. 3). Since nearly all of the released H_2S is precipitated, R_{FeS} simply reflects the increase of R_{SO_4}-CH_4 over time. (2) The reactivity of H_2S towards $Fe(III)_{relict}$ ($R_{Fe(III)relict}$ are about one order of magnitude lower than $R_{Fe(III)react}$) limits the increase of H_2S concentrations, where $Fe(III)_{react}$ is already consumed. (3) $R_{Fe(III)relict}$ will slightly raise as H_2S concentrations in the pore-water increase, thus limiting the further increase of H_2S concentrations.

Given all advantages and limitations of this approach, the major errors result from uncertainties of the starting conditions and the amount of reactive Fe(III) minerals. Although in balance with the FeS enrichment (after conversion), the average concentration of 4 g kg^{-1} may have slightly varied within the limits as observed below 6 m (Fig. 8b). Both factors together may sum up to an error of ~1000 yr. However, compared to a sediment age at 4 m depth of otherwise 40000 and 80000 (based on normal sedimentation rates) this does not affect the general outcome of this approach.

3.6. Quantification of SO_4 Fluxes

Finally, we want to address the quantitative aspects of the AOM-related depletion of SO_4. As shown in Table 1, we calculated the SO_4 penetration depth and the resulting diffusive SO_4 (and CH_4) fluxes for the whole area using the complete data set of 23 gravity cores. The regional distribution of both SO_4 penetration depth and SO_4 flux is obtained by applying a simple nearest-neighbor gridding method as shown in Figure 10. Although the zone of AOM was not reached in a number of cores we can assume that the general pattern is not essentially changed. This assumption is even more supported by the fact that those areas with high SO_4 penetration depths (=low SO_4 fluxes) are less affected by sedimentary events (lower supply with mineralizable material) and thus, steady state pore-water conditions are more likely. Additionally, the general SO_4 flux pattern agrees well with the one of benthic nutrient fluxes driven by surface mineralization processes (Hensen et al., 2000). Overall, we calculated that 6.6×10^{10} mol SO_4 (or S) are annually consumed by the process of AOM within a total area of 2.46×10^6 km^2 (excluding the shelf areas above 200 m water depth), which is ~0.7% of the global sea floor area. To estimate, whether this amount has a general importance in terms of global sulfur budgets, we projected the total annual flux to the global area of the continental slope and rise (1.02×10^8 km^2; Middelburg et al., 1993), which sums up to ~2.6×10^{12} mol SO_4. This method might overestimate the global importance due to the more intense downslope transport of reactive material in the Argentine Basin compared to other regions of the ocean. However, this effect might be reduced since also sediments below high productivity regions are included in this calculation with comparable fluxes of SO_4 (and CH_4) into the zone of AOM are reported (e.g., D'Hondt et al., 2002; Niewöhner et al., 1998). Canfield (1991) estimated the global sulfate reduction by organic matter degradation in surface sediments to be ~3.7×10^{13} mol yr^{-1}. In comparison to our result this means that sulfate reduction by AOM makes up as much as 7% of the global sulfate reduction occurring in surface sediments.

Pore-water and solid phase data presented above are indicative for a quantitative fixation of H_2S released by AOM. Additional data reported from other deep-sea environments also show that varying, but significant, amounts of H_2S produced in the zone of AOM are subsequently fixed in the sediments (Schulz et al., 1994; Kasten et al., 1998; Niewöhner et al., 1998; Adler et al., 2000; Jørgensen et al., 2001; Zabel and Schulz, 2001). In this context Passier et al. (1996) highlighted the significance of sapropel-related downward pyritization compared to limited in situ precipitation. Furthermore, in the deep-water environments of concern the AOM-related fixation of H_2S usually occurs in several meters of sediment depth (D'Hondt et al., 2002), thus, a subsequent re-oxidation of once precipitated sulfides is more unlikely as in surface sediments. Since Fe(III) minerals are ubiquitously available along the continental margins around the world these facts suggest that AOM-related sulfur fixation might be of global significance in terms of sulfur burial in marine sediments.

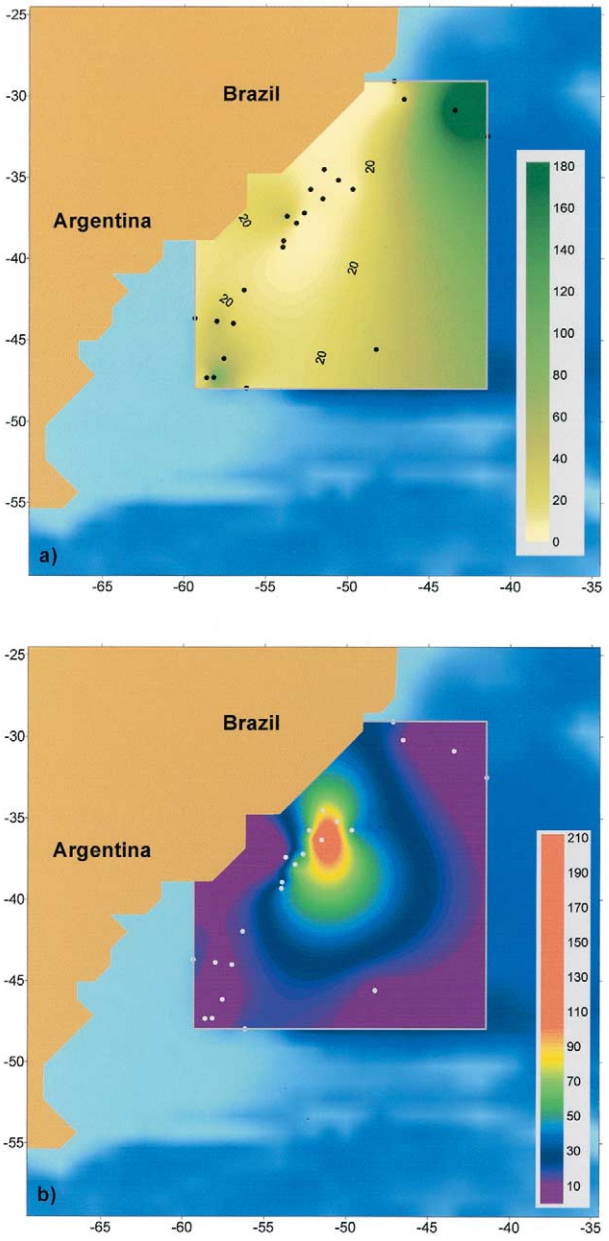

Fig. 10. Distribution maps of the SO_4 penetration depth in m (a) and the diffusive SO_4 fluxes in mmol $m^{-2}yr^{-1}$ into the SMT (b). The grid is based on the data of all 23 gravity cores as listed in Table 1. The fluxes are highest (shallow SO_4 penetration) in front of the Rio de Plata mouth. Due to the dynamic sedimentary environment there exists no water depth relation. This observation is in agreement with results from studies of surface sediment mineralization (Hensen et al., 2000) and distribution of diatom assemblages (Romero and Hensen, 2002). The overall SO_4 flux in the study area (2.46×10^6 km^2) is 6.6×10^{10} mol yr^{-1} for water depths >200m.

The burial of reduced sulfur is one of the major driving forces controlling the atmospheric oxygen levels over time (Paytan et al., 1998; Petsch and Berner, 1998; Berner, 2001), thus changes in the rates of AOM might as well affect this important coupling. Global marine burial rates of reduced sulfur were e.g., calculated by Berner (1982) based on a compilation of organic carbon burial rates and average C_{org}/S weight ratios. Accordingly, the average C_{org}/S value for normal marine surface sediments is ~3 (Berner, 1982; Berner and Canfield, 1989). Decreased C_{org}/S ratios due to an allochthonous source of S as observed in this study (Figs. 5 and 8d) are a widespread phenomenon, i.e., (Passier et al., 1996; Kasten et al., 1998) enhancing preferential sulfur burial similar to processes under euxinic conditions (Raiswell and Berner, 1985; Berner and Canfield, 1989).

Overall, Berner (1982) estimated the total burial of pyritic sulfur to be $\sim 1.2 \times 10^{12}$ mol yr^{-1}. About 50% lower values for the major part of the Phanerozoic were calculated by Berner and Canfield (1989) who applied a mathematical model to study the variations of atmospheric oxygen levels driven by burial and weathering rates of organic carbon and reduced sulfur. Overall, those values are ~2–5 times less than our projected SO_4 flux, which only implies continental margin areas without shelves. The SO_4 flux calculated for the Argentine Basin alone would thus be ~5% of the global sulfur burial (on less than 1% of the surface area). Even if the fixation of the sulfur may be limited by the availability of reactive iron phases and yet not be quantitative, there is striking evidence for the importance of this process. Even though higher a variability of this parameter was tested in more recent models (Berner and Petsch, 1998; Petsch and Berner, 1998) the obvious potential of AOM for the drawdown of seawater SO_4 and S-burial obviously deserves more explicit consideration in long-term models on geochemical cycles.

Further significance of enhanced AOM-related sulfide precipitation in marine sediments comes from a recent study of (Jørgensen et al., personal communication), who demonstrated that strongly δ^{34}-enriched pyrite with can be produced in a sediment open to diffusion. Since δ^{34}S in surface sediments are generally strongly depleted (Habicht and Canfield, 1996) the quantitative significance of the opposite effect may be an important future topic.

4. CONCLUSIONS

The major results of the study can be summarized as follows:

Persistent downslope transport of large amounts of sediments in the western Argentine Basin creates transient geochemical conditions on timescales between years and thousands of years.

The observed variety of SO_4 profiles can exceptionally be related to the occurrence of depositional events and changes in the CH_4 flux. If CH_4 is available in sufficient amounts AOM is the dominant process of SO_4 depletion in the pore-waters.

Different scenarios have shown, how transport and reaction modeling can be used to explain process interactions of rapid sedimentation, chemical reaction, and diffusion and how this can be used for the timing of sedimentary events.

The importance of AOM in terms of global budgets of sulfur has obviously been underestimated until present. The fact that AOM controlled sulfur burial might override the total sulfur burial in marine sediments obviously requires a revision of the marine sulfur budget on a global scale. As there is a large impact of the sulfur burial on the atmospheric oxygen level this finding has probably to be considered in global geochemical models.

Acknowledgments—This study is based on the extensive fieldwork during two cruises with RV *Meteor* with was strongly supported by the crews and other cruise participants (i.e., PARASOUND guards). For technical assistance on board ship and in the home laboratory we are indebted to Sigrid Hinrichs, Karsten Enneking, Susanne Siemer, and Markus Schmidt. Physical properties data have been kindly provided by the Marine Geophysics Group (Prof. U. Bleil) at Bremen University, Department of Geosciences. For very helpful comments on an earlier draft we thank Anja Reitz. The manuscript greatly benefited from very detailed evaluations of an anonymous reviewer and the associate editor Jack Middelburg. This work was funded by the Deutsche Forschungsgemeinschaft (Sonderforschungsbereich 261 at Bremen University, contribution No. 355; RCOM0048).

Associate editor: J. Middelburg

REFERENCES

Adler M., Hensen C., Kasten S., and Schulz H. D. (2000) Computer simulation of deep sulfate reduction in sediments of the Amazon Fan. *Int. J. Earth Sci.* **88**, 641–654.

Adler M., Hensen C., Wenzhöfer F., Pfeifer K., and Schulz H. D. (2001) Modeling of calcite dissolution by oxic respiration in supralysoclinal deep-sea sediments. *Mar. Geol.* **177**, 167–189.

Antoine D., André J.-M., and Morel A. (1996) Oceanic primary production: 2. Estimation at global scale from satellite (coastal zone color scanner) chlorophyll. *Glob. Biogeochem. Cycles* **10**, 57–69.

Behrenfeld M. J. and Falkowski P. G. (1997) Photosynthetic rates derived from satellite-based chlorophyll concentration. *Limnol. Oceanogr.* **42**, 1–20.

Berner R. A. (1982) Burial of organic carbon and pyrite sulfur in the modern ocean: Its geochemical and environmental significance. *Am. J. Sci.* **282**, 451–473.

Berner R. A. (2001) Modeling atmospheric O_2 over Phanerozoic time. *Geochim. Cosmochim. Acta* **65**, 685–694.

Berner R. A. and Canfield D. E. (1989) A new model for atmospheric oxygen over phanerozoic time. *Am. J. Sci.* **289**, 333–361.

Berner R. A. and Petsch S. T. (1998) The sulfur cycle and atmospheric oxygen. *Science* **282**, 1426–1427.

Bleil U. and participants. (1994) Report and preliminary results of *Meteor* cruise M 29/2 Montevideo–Rio de Janeiro, 15.07.–08.08. 1994, Vol. 59, p. 153. Fachbereich Geowissenschaften, Universität Bremen.

Boesen C. and Postma D. (1988) Pyrite formation in anoxic environments of the Baltic. *Am. J. Sci.* **288**, 575–603.

Boetius A., Ravenschlag K., Schubert C. J., Rickert D., Widdel F., Giesecke A., Amann R., Jørgensen B. B., Witte U., and Pfannkuche O. (2000) A marine microbial consortium apparently mediating anaerobic oxidation of methane. *Nature* **407**, 623–626.

Borowski W. S., Paull C. K., and Ussler W. (1996) Marine pore-water sulfate profiles indicate in situ methane flux from underlying gas hydrate. *J. Geol.* **24**, 655–658.

Borowski W. S., Paull C. K., and Ussler W. III. (1997) Carbon cycling within the upper methanogenic zone of continental rise sediments: An example from the methane-rich sediments overlying the Blake Ridge gas hydrate deposits. *Mar. Chem.* **57**, 299–311.

Borowski W. S., Paull C. K., and Ussler W. III. (1999) Global and local variations of interstitial sulfate gradients in deep-water, continental margin sediments: Sensitivity to underlying methane and gas hydrates. *Mar. Geol.* **159**, 131–154.

Boudreau B. P. (1997) *Diagenetic Models and Their Implementation: Modelling Transport and Reactions in Aquatic Sediments.* Springer.

Canfield D. E. (1991) Sulfate reduction in deep-sea sediments. *Am. J. Sci.* **291**, 177–188.

Canfield D. E., Raiswell R., and Bottrell S. (1992) The reactivity of sedimentary iron minerals toward sulfide. *Am. J. Sci.* **292**, 659–683.

Dawson A. G., Long D., and Smith D. E. (1988) The Storegga Slides: Evidence from eastern Scotland for a possible tsunami. *Mar. Geol.* **82**, 271–276.

De Lange G. J. (1983) Geochemical evidence of a massive slide in the southern Norwegian Sea. *Nature* **305**, 420–422.

D'Hondt S., Rutherford S., and Spivack A. J. (2002) Metabolic activity of subsurface life in deep-sea sediments. *Science* **295**, 2067–2070.

Dickens G. R. (2001) Sulfate profiles and barium fronts in sediment on the Blake Ridge: Present and past methane fluxes through a large gas hydrate reservoir. *Geochim. Cosmochim. Acta* **65**, 529–543.

Egeberg P. K. and Dickens G. R. (1999) Thermodynamic and pore-water halogen constraints on gas hydrate distribution at ODP Site 997 (Blake Ridge). *Chem. Geol.* **153**, 53–79.

Ewing M., Ludwig W. J., and Ewing J. I. (1964) Sediment distribution in the oceans: The Argentine Basin. *J. Geophys. Res.* **69**, 2003–2033.

Ewing M., Eittreim S. L., Ewing J. I., and LePichon X. (1971) Sediment transport and distribution in the Argentine Basin 3. Nepheloid layer and processes of sedimentation. *Phys. Chem. Earth.* **8**, 51–76.

Ferdelman T. G., Lee C., Pantoja S., Harder J., Bebout B. M., and Fossing H. (1997) Sulfate reduction and methanogenesis in a Thioploca-dominated sediment off the coast of Chile. *Geochim. Cosmochim. Acta* **61**, 3065–3079.

Ferdelman T. G., Fossing H., Neumann K., and Schulz H. D. (1999) Sulfate reduction in surface sediments of the southeast Atlantic continental margin between 15°38′S and 27°57′S (Angola and Namibia). *Limnol. Oceanogr.* **44**, 650–661.

Föllmi K. B. (1996) The phosphorus cycle, phosphogenesis and marine phosphate-rich deposits. *Earth-Sci. Rev.* **40**, 55–124.

Fossing H., Ferdelman T. G., and Berg P. (2000) Sulfate reduction and methane oxidation in continental margin sediments influenced by irrigation (South-East Atlantic off Namibia). *Geochim. Cosmochim. Acta* **64**, 897–910.

Garzoli S. R. (1993) Geostrophic velocity and transport variability in the Brazil-Malvinas Confluence. *Deep-Sea Res. I* **40**, 1379–1403.

Gordon A. L. (1989) Brazil-Malvinas Confluence—1984. *Deep-Sea Res. II* **36**, 359–384.

Grant J. A. and Schreiber R. (1990) Modern swathe sounding and sub-bottom profiling technology for research applications: The Atlas Hydrosweep and Parasound systems. *Mar. Geophys. Res.* **12**, 9–19.

Grasshoff K., Ehrhardt M., and Kremling K. (1983) *Methods of Seawater Analysis.* Verlag Chemie.

Güchter R., Meyer J. S., and Mares A. (1988) Contribution of bacteria to release and fixation of phosphorus in lake sediments. *Limnol. Oceanogr.* **33**, 1542–1558.

Habicht K. S. and Canfield D. E. (1996) Sulphur isotope fractionation in modern microbial mats and the evolution of the sulphur cycle. *Nature* **382**, 342–343.

Haese R. R., Wallmann K., Dahmke A., Kretzmann U., Müller P. J., and Schulz H. D. (1997) Iron species determination to investigate early diagenetic reactivity in marine sediments. *Geochim. Cosmochim. Acta* **61**, 63–72.

Haese R. R., Schramm J., Rutgers van der Loeff M. M., and Schulz H. D. (2000) A comparative study of iron and manganese diagenesis in continental slope and deep sea basin sediments off Uruguay (SW Atlantic). *Int. J. Earth Sci.* **88**, 619–629.

Hensen C., Landenberger H., Zabel M., and Schulz H. D. (1998) Quantification of diffusive benthic fluxes of nitrate, phosphate and silicate in the southern Atlantic Ocean. *Glob. Biogeochem. Cycles* **12**, 193–210.

Hensen C., Zabel M., and Schulz H. D. (2000) A comparison of benthic nutrient fluxes from deep-sea sediments off Namibia and Argentina. *Deep-Sea Res. II* **47**, 2029–2050.

Hensen C., Pfeifer K., Wenzhöfer F., Volbers A., Schulz S., Romero O., and Seiter K. (in press) Fluxes at the benthic boundary layer—A global view from the South Atlantic. In *The South Atlantic in the Late Quaternary* (eds. G. Wefer, S. Mulitza, and C. Rühlemann). Springer.

Hinrichs K. U., Hayes J. M., Sylva S. P., Brewer P. G., and DeLong E. F. (1999) Methane-consuming archaebacteria in marine sediments. *Nature* **398**, 802–805.

Hoehler T. M., Alperin M. J., Albert D. B., and Martens C. S. (1994) Field and laboratory studies of methane oxidation in an anoxic marine sediment: Evidence for a methanogen-sulfate reducer consortium. *Glob. Biogeochem. Cycles* **8**, 451–463.

Iversen N. and Jørgensen B. B. (1985) Anaerobic methane oxidation rates at the sulfate-methane transition in marine sediments from Kattegat and Skagerrak (Denmark). *Limnol. Oceanogr.* **30**, 944–955.

Jørgensen B. B. (1977) The sulfur cycle of a coastal marine sediment (Limfjorden, Denmark). *Limnol. Oceanogr.* **22**, 814–832.

Jørgensen B. B., Weber A., and Zopfi J. (2001) Sulfate reduction and anaerobic methane oxidation in Black Sea sediments. *Deep Sea Res. I* **48**, 2097–2120.

Kasten S., Freudenthal T., Gingele F. X., von Dobeneck T., and Schulz H. D. (1998) Simultaneous formation of iron-rich layers at different redox boundaries in sediments of the Amazon Deep-Sea Fan. *Geochim. Cosmochim. Acta* **62**, 2253–2264.

Kasten S., Heuer V., Zabel M., and Hensen C. (in press) Nonsteady-state diagenesis and its documentation and preservation in marine sediment/pore-water systems. In *The South Atlantic in the Late Quaternary* (eds. G. Wefer, S. Mulitza, and C. Rühlemann). Springer.

Ledbetter M. T. and Klaus A. (1987) Influence of bottom currents on sediment texture and sea-floor morphology in the Argentine Basin. In *Geology and Geochemistry of Abyssal Plains*, Vol. 31 (eds. P. P. E. Weaver and J. Thomson), pp. 23–31. Geological Society Special Publication.

Lee S. H., Chough S. K., Back G. G., Kim Y. B., and Sung B. S. (1999) Gradual downslope change in high-resolution acoustic characters and geometry of large-scale submarine debris lobes in Ulleung Basin, East Sea (Sea of Japan), Korea. *Geo-Mar. Lett.* **19**, 254–261.

Lucotte M., Mucci A., Hillaire-Marcel C., and Tran S. (1994) Early diagenetic processes in deep Labrador Sea sediments: Reactive and nonreactive iron and phosphorus. *Can. J. Earth Sci.* **31**, 14–27.

Mach D. L., Ramirez A., and Holland H. D. (1987) Organic phosphorus and carbon in marine sediments. *Am. J. Sci.* **278**, 429–441.

Manley P. L. and Flood R. D. (1989) Anomalous sound velocities in near-surface, organic-rich, gassy sediments in the central Argentine Basin. *Deep-Sea Res.* **36**, 611–623.

Michaelis W., Seifert R., Nauhaus K., Treude T., Thiel V., Blumenberg M., Knittel K., Gieseke A., Peterknecht K., Pape T., Boetius A., Amann R., Jørgensen B. B., Widdel F., Peckmann J., Pimenov N. V., and Gulin M. B. (2002) Microbial reefs in the Black Sea fueled by anaerobic oxidation of methane. *Science* **297**, 1013–1015.

Middelburg J. J. (1991) Organic carbon, sulphur, and iron in recent semi-euxinic sediments of Kau Bay, Indonesia. *Geochim. Cosmochim. Acta* **55**, 815–828.

Middelburg J. J., Calvert S. E., and Karlin R. (1991) Organic-rich transitional facies in silled basins: Response to sea-level change. *Geology* **19**, 679–682.

Middelburg J. J., Vlug T., and Van der Nat F. J. W. A. (1993) Organic matter mineralization in marine systems. *Glob. Planet. Change.* **8**, 47–58.

Niewöhner C., Hensen C., Kasten S., Zabel M., and Schulz H. D. (1998) Deep sulfate reduction completely mediated by anaerobic methane oxidation in sediments of the upwelling area off Namibia. *Geochim. Cosmochim. Acta* **62**, 455–464.

Passier H. F., Middelburg J. J., Van Os B. J. H., and De Lange G. J. (1996) Diagenetic pyritisation under eastern Mediterranean sapropels caused by downward sulphide diffusion. *Geochim. Cosmochim. Acta* **60**, 751–763.

Passier H. F., Middelburg J. J., De Lange G. J., and Böttcher M. E. (1999) Modes of sapropel formation in the eastern Mediterranean: Some constrains based on pyrite properties. *Mar. Geol.* **153**, 199–219.

Paytan A., Kastner M., Campbell D., and Thiemes M. H. (1998) Sulfur isotopic composition of Cenozoic seawater sulfate. *Science* **282**, 1459–1462.

Peterson R. G. and Stramma L. (1991) Upper-level circulation in the South Atlantic Ocean. *Progr. Oceanogr.* **26**, 1–73.

Peterson R. G., Johnson C. S., Krauss W., and Davis R. E. (1996) Langrangian measurements in the Malvinas Current. In *The South Atlantic: Present and Past Circulation* (eds. G. Wefer, W. H. Berger, G. Siedler, and D. J. Webb), pp. 239–247. Springer.

Petsch S. T. and Berner R. A. (1998) Coupling the geochemical cycles of C, P, Fe, and S: The effect on atmospheric O_2 and the isotopic records of carbon and sulfur. *Am. J. Sci.* **298**, 246–262.

Pruysers P. A. (1998) Early diagenetic processes in sediments of the Angola Basin, eastern South Atlantic. Ph.D. thesis. Utrecht University.

Pruysers P. A., De Lange G. J., Middelburg J. J., and Hydes D. J. (1993) The diagenetic formation of metal-rich layers in sapropel-containing sediments in the eastern Mediterranean. *Geochim. Cosmochim. Acta* **57**, 527–536.

Raiswell R. and Berner R. A. (1985) Pyrite formation in euxinic and semi euxinic sediments. *Am. J. Sci.* **285**, 710–724.

Reid J. L. (1989) On the total geostrophic circulation of the South Atlantic Ocean: Flow patterns, tracers, and transports. *Prog. Oceanogr.* **23**, 149–244.

Richardson M. J., Weatherly G. L., and Gardner W. D. (1993) Benthic storms in the Argentine Basin. *Deep Sea Research II* **40**, 975–987.

Romero O. and Hensen C. (2002) Oceanographic control of biogenic opal and diatoms in surface sediments of the South Western Atlantic. *Mar. Geol.* **186**, 263–280.

Schulz H. D., Dahmke A., Schinzel U., Wallmann K., and Zabel M. (1994) Early diagenetic processes, fluxes, and reaction rates in sediments of the South Atlantic. *Geochim. Cosmochim. Acta* **58**, 2041–2060.

Segl M. and participants. (1994) Report and preliminary results of *Meteor* cruise M 29/1 Montevideo-Montevideo, 16.06.–13.07. 1994, Vol. **58,** pp. 94. Fachbereich Geowissenschaften, Universität Bremen.

Spiess V. (1993) *Digitale Sedimentechographie—Neue Wege zu einer hochauflösenden Akustostratigraphie*. Fachbereich Geowissenschaften, Universität Bremen.

Suess E., Torres M. E., Bohrmann G., Collier R. W., Greinert J., Linke P., Rehder G., Trehu A., Wallmann K., Winckler G., and Zuleger E. (1999) Gas hydrate destabilization: Enhanced dewatering, benthic material turnover and large methane plumes at the Cascadia convergent margin. *Earth Planet. Sci. Lett.* **170**, 1–15.

Thamdrup B. (2000) *Bacterial Manganese and Iron Reduction in Aquatic Sediments,* Vol. 16 (ed. B. Schink). Kluwer Academic/Plenum.

Thomson J., Wilson T. R. S., Culkin F., and Hydes D. J. (1984) Non-steady state diagenetic record in eastern equatorial Atlantic sediments. *Earth Planet. Sci. Lett.* **71**, 23–30.

Thomson J., Higgs N. C., Wilson T. R. S., Croudace I. W., De Lange G. J., and Van Santvoort P. J. M. (1995) Redistribution and geochemical behaviour of redox-sensitive elements around S1, the most recent eastern Mediterranean sapropel. *Geochim. Cosmochim. Acta* **59**, 3487–3501.

Van Santvoort P. J. M., De Lange G. J., Thomson J., Cussen H., Wilson T. R. S., Krom M. D., and Ströhle K. (1996) Active post-depositional oxidation of the most recent sapropel (S1) in sediments of the eastern Mediterranean Sea. *Geochim. Cosmochim. Acta* **60**, 4007–4024.

Wenzhöfer F., Adler M., Kohls O., Hensen C., Strotmann B., Boehme S., and Schulz H. D. (2001) Calcite dissolution driven by benthic mineralization in the deep-sea: In situ measurements of Ca^{2+}, pH, pCO_2, O_2. *Geochim. Cosmochim. Acta* **65**, 2677–2690.

Wilson T. R. S., Thomson J., Colley S., Hydes D. J., Higgs N. C., and Sørensen J. (1985) Early organic diagenesis: The significance of progressive subsurface oxidation fronts in pelagic sediments. *Geochim. Cosmochim. Acta* **49**, 811–822.

Wilson T. R. S., Thomson J., Hydes D. J., Colley S., Culkin F., and Sørensen J. (1986) Oxidation fronts in pelagic sediments: Diagenetic formation of metal-rich layers. *Science* **232**, 972–975.

Wilson T. R. S. and Thomson J. (1998) Calcite dissolution accompanying early diagenesis in turbiditic deep ocean sediments. *Geochim. Cosmochim. Acta* **62**, 2087–2096.

Wilson H. R. and Rees N. W. (2000) Classification of the mesoscale features in the Brazil-Falkland Current confluence zone. *Progr. Oceanogr.* **45**, 415–426.

Wynn R. B., Masson D. G., Stow D. A. V., and Weaver P. P. E. (2000) The Northwest. African slope apron: A modern analogue for deep-water systems with complex seafloor topography. *Mar. Petrol. Geol.* **17**, 253–265.

Young R. W. and Bryant, E. A. (1992) Catastrophic wave erosion on the southeastern coast of Australia: Impact of the Lanai tsunamis ca. 105 ka? *Geology* **20,** 199–202.

Zabel M. and Schulz H. D. (2001) Importance of submarine landslides for non-steady state conditions in pore-water systems—Lower Zaire (Congo) deep-sea fan. *Mar. Geol.* **176**, 87–99.